Design, Fabrication, and Characterization of a Thin-Film Nickel-Titanium Shape Memory Alloy Diaphragm for Use in Micro-Electro-Mechanical Systems

A Thesis Presented to the Faculty of California Polytechnic State University, San Luis Obispo

In Partial Fulfillment of the Requirements for the Degree Master of Science in General Engineering with Emphasis in Materials Engineering

By

Brian Joel Alvarez

August 26, 2011

Committee Membership

Title: Design, Fabrication, and Characterization of a Thin-Film Nickel-Titanium Shape Memory Alloy Diaphragm for Use in Micro-Electro-Mechanical Systems

Author: Brian Joel Alvarez

Date Submitted: August 26, 2011

Committee Chair: Dr. Richard Savage, Materials Engineering Professor

Committee Member: Dr. Linda Vanasupa, Materials Engineering Professor

Committee Member: Dr. David Clague, Biomedical Engineering Professor

Abstract

Design, Fabrication, and Characterization of a Thin-Film Nickel-Titanium Shape Memory Alloy Diaphragm for Use in Micro-Electro-Mechanical Systems

Brian Joel Alvarez

Previous work done at Cal Poly has shown that thin-film nickel-titanium (NiTi) can be easily sputtered onto silicon wafers and annealed to create a crystallized shape memory alloy (SMA) film. Initial work on creating devices yielded cantilevers that were highly warped due to thin-film stress created during the sputtering process. The objective of this work was to create a thin-film NiTi SMA device that could be better characterized. A membrane was selected due to the simplicity of fabrication and testing which would also oppose the thin-film stress due to the increase in attachment points to the substrate.

Silicon wafers were etched through the majority of the thickness (~75%) creating square etch pits of varying sizes varying from 1294 µm to 4394 µm. The wafers were then sputtered with an approximate NiTi film of 5 µm followed by a thin chromium film. The chromium film would act as a diffusion barrier and prevent oxygen from diffusing into the NiTi and reacting with the titanium and forming titanium dioxide. These wafers were then annealed in a custom built vacuum annealing chamber at 550 °C for 1 hour with a pressure around 77 kPa. The chromium was then etched away followed by the remaining silicon. This left a thin membrane of shape memory NiTi which was packaged in order for characterization. The devices were glued to an aluminum substrate using

polydimethylsiloxane (PDMS) and sealed with a small Tygon tube leading to the sealed chamber.

This packaged device was then able to be pressurized using a nitrogen tank and the resulting NiTi membrane deflection was measured using a profilometer. Due to the differences in elastic moduli of the room temperature phase (martensite) and the high temperature phase (austenite) a difference of deflection was expected. The austenite finish (A_f) temperature of bulk NiTi films was found to be around 60 °C so the devices were tested at both room temperature and at 60 °C. After testing seven separate devices of varying sizes, a regression model was used to analyze the final data.

It was found that pressure, membrane size and theoretical versus actual deflection all affected the maximum deflection, but temperature did not. Higher pressures and larger membranes led to higher deflections as membrane deflection models from fundamental principles indicated. Some devices showed inferior performance when compared to the model due to incomplete silicon etching which caused lower deflection due to the much higher modulus of the remaining silicon. Thickness could also limit the amount of deflection measured with a thicker film leading to less deflection, but this is likely not the case due to the high uniformity of the sputtering system. Other devices showed superior performance over the model most likely due to either local delamination or lateral silicon etching. Both these would create a membrane that was larger than expected leading to a higher deflection. Unforutnaly, differential scanning calorimetry (DSC) analysis showed no shape memory behavior on a test wafer which was anneald at 550 ˚C for 1 hour. A design of experiments was conducted in order to find a heat treatment that would anneal the NiTi film and ensure that shape memory behavior could be obtained. An annealing at

650 °C for 1 hour showed a sharper and clearer A_f phase transformation at around the target temperature of 60 °C. Annealing a full wafer at this temperature and time also showed that no delamination would occur which has also been linked to nonideal behavior of the NiTi membranes which has also been linked to meaningful behavior of the NiTi membranes.

Keywords: MEMS, NiTi, Shape Memory Alloy, Diaphragm, Thin-film, Sputtering, Vacuum Annealing, Micropumps

Acknowledgements

I would like to acknowledge the assistance, knowledge and guidance of my adviser Dr. Richard Savage. His knowledge in the various microfabrication processes as well as ability to troubleshoot the equipment were invaluable to the completion of my project. Also, his ability to always question why my results were meaningful kept me thinking about the broader impact of my project.

I would also like to thank my committee Dr. Linda Vanasupa and Dr. David Clague for bringing their unique perspectives, experiences and knowledge to my project.

I would like to also acknowledge Dr. Ray Fernando, Jeff Foster, and the Chemistry Department for their assistance and allowing me to use the DSC.

I want to thank all of the other graduate students in the materials department and Microsystems Technology Group most notability: Josh Angell, Adam Olzick, Patrick Hyland, Tim McCrone, and Mike Marrujo for listening to my problems and always being willing to help me through my project in the worst and best times.

Lastly, I would like to thank all my friends and family who have always been there for me and made my college experience outstanding.

Table of Contents

List of Tables

List of Equations

List of Figures

Chapter 1 - Introduction

1.1 Micro-Electro-Mechanical Systems

Micro-electro-mechanical systems (MEMS) are a relatively new and growing field in which bulk products can be scaled down to the micrometer scale. The ability to use microfabrication techniques originally developed to create integrated circuits can be used to create these miniature devices. Microfabrication techniques allow for precise control over surface microarchitecture, topography, and feature size using techniques like thin-film deposition, photolithography, and etching. MEMS applications are seen everywhere from accelerometers like those found in airbag deployment systems for vehicles to inkjet printers, to digital-light projection systems and optical switching.[27]

BioMEMS is a subfield that is growing rapidly due to the size of the devices produced which are on the same scale as cells. BioMEMS have found applications in both research and therapeutic applications ranging from DNA sequencing, cell encapsulation, biosensors, chemical analysis systems and drug delivery.[1] Many other applications are currently being researched to be used in the field of microfluidics.

1.2 MEMS, BioMEMS & Microfluidics

One of the fastest growing fields within MEMS and bioMEMS is microfluidics, where these small devices can sense, pump, mix, monitor and control small amounts of fluid. This is seen often in conjunction with biomedical engineering where processes like chemical sensing, drug delivery, molecular separation, and environmental monitoring can be miniaturized saving both time and material usage.[2] Microfabrication techniques have

allowed for the ability to precisely tailor size, shape, number, volume, openings, and surface characteristics of devices.[3] This leads to the ability to directly send a specific amount of drug to the site, which will increase the therapeutic effectiveness while reducing the risk of over-dosage.[3] Most drugs have a range of concentration where they are most efficient; above which can be toxic and below which will yield no therapeutic effect (Figure 1).[1] Integrated drug delivery systems are being researched which are able to give fine control at low flow rates (1-10 μL/min) and are less expensive and much smaller than traditional drug delivering pumps.[1] Many of these systems are also implantable which enables local drug delivery and long-term dosing which helps to alleviate infection and contamination.[1] Researchers are also looking at using MEMS to release drugs in a pulsated format which would be a much more controlled version of traditional time-release drug delivery (Figure 2). Some drugs work best when small amounts are released at a time, and so a continuous release would not work.[4] Both these drug delivery methods require microfluidic pumps that are extremely repeatable. Both the controlled and pulsated formats lead to drug delivery profile that maximizes the time in the therapeutic zone, but both achieve it in different ways and the preferred method for drug delivery depends on a many variables like type of drug and dosage.

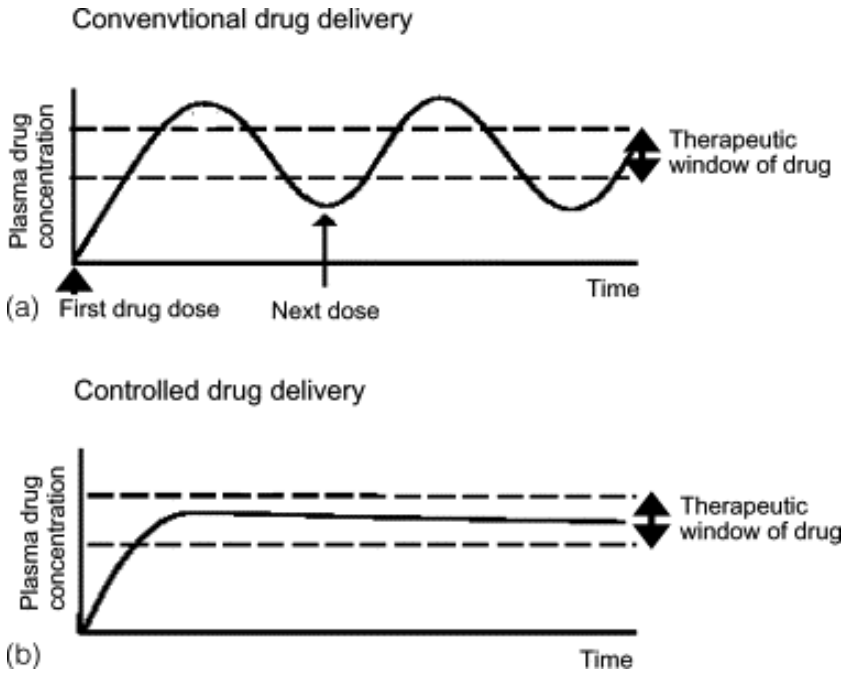

Figure 1: a) Conventional time-release drug delivery system with the traditional "hill and valley" profile versus b) controlled drug delivery profile commonly found with the use of micropumps.[5] Controlled allows the drug concentration to remain within the therapeutic window much longer than traditional methods.[5]

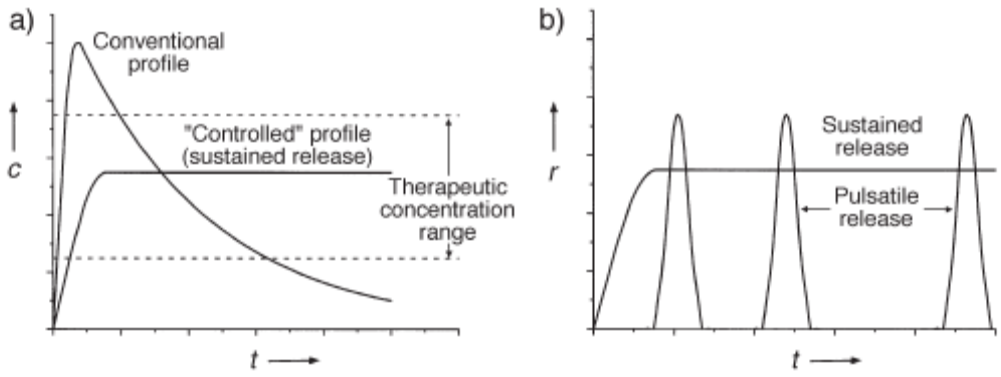

Figure 2: a) Conventional profile versus a controlled profile showing the more desired profile maximizes the time within the therapeutic range. b) Continued release versus pulsated release profiles.[4]

1.3 Micropumps

Integrated drug delivery systems are complex systems where reservoirs, micropumps, valves, microsensors, microchannels and other parts are connected in a circuit-like design (Figure 3). Micropumps are an essential piece of the drug delivery system. A micropump can consist of microreservoirs, microchannels, microfilters, and valves for the precise movement of fluids through the system.[2]

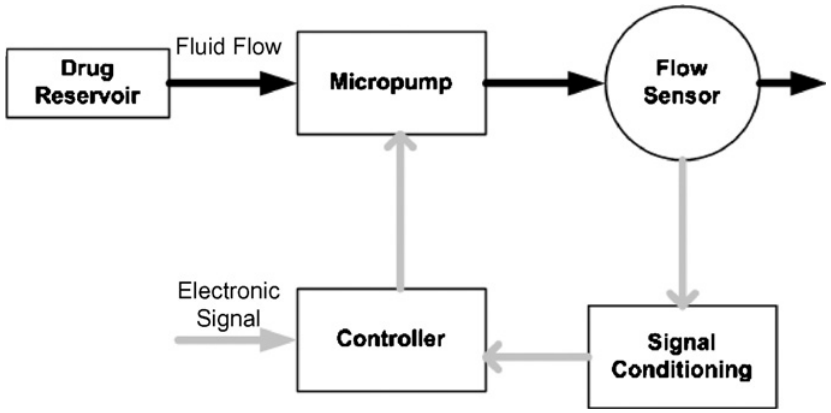

Figure 3: Schematic showing a generic drug delivery system.[2]

There are two main types of micropumps: mechanical and non-mechanical (Table I); the former consists of a moving diaphragm and check valves while the latter does not. The most common types of non-mechanical micropumps are magnetohydrodynamic, electrohydrodynamic, electroosmotic, electrowetting, bubble type, flexural planar wave, electrochemical and evaporation.[2] There are many ways to actuate the pumping diaphragm for the mechanical pumps, but the most common are electrostatic, piezoelectric, thermopneumatic, shape memory alloy, bimetallic, electromagnetic and phase change.[2] These are also called displacement pumps and they are actuated with a flexible membrane.[2] The fluid flow is achieved by the deflection of the membrane

creating a pressure difference causing fluid flow.[2] Each type of actuation or pumping system has their respective advantages and disadvantages are listed in Table I.

Table I: Comparison of various mechanical and non-mechanical micropumps with ranges.[6]

Pumping Principle	Voltage (V)	Max Flow Rate (μL/min)	Max Pressure (MPa)
Electrostatic	200	30-850	0.02-0.31
Piezoelectric	110-350	13.33-1900	0.001-0.35
Thermopneumatic	8-15	9-44	0.0025-0.016
Shape Memory Alloy	0.6-8	50-700	0.0005-0.1
Bimetallic	5.5-16	43-44	0.107
Magnetohydrodynamic	4-60	2.88-63	0.1037
Electrohydrodynamic	300-700	14	0.0007-0.0025
Electroosmotic	1000-5000	1.75-15	0.0334-2.036
Electrochemical	1.5-4.5	0.024-0.08	0.0235-0.11
Osmotic	0	0.0033	n/a
Capillary	0	7.2	0.0065
Electrowetting	2.3	70	0.0008

1.4 Shape Memory Micropumps

Shape memory alloy micropumps use the shape memory effect to cause a displacement in a mechanically constrained membrane.[2] The low temperature phase, martensite, is ductile and is able to deform large amounts. When heated the martensite phase changes to the higher temperature phase, austenite. This phase change returns the material back to the original shape if it is not mechanically constrained, but if it is the material applies a large force in order to attempt to return to its original form (Figure 4). High voltages and currents which lead to high power consumption and slow response time are some of the problems of shape memory micropumps but it is able to deform large amounts yielding high head pressures while having relatively large work densities.[2] Complex flow patterns and high flow resistance require high head pressures but can be

overcome by using shape memory alloy actuation.[7] The recoverable strain has been reported from 6-8%.[8] The higher strain values shape memory devices lead to higher deflections which in turn lead to higher obtainable head pressures. Work densities have also been reported ranging from 6.0 X 10^6 to 2.5 X 10^7 J/m^3 which is much higher than piezoelectric materials which only have work densities around 0.25 X 10^6 J/m^3.[9] The most common shape memory alloys for micropump actuation are Au/Cu, In/Ti, and Ni/Ti.[2]

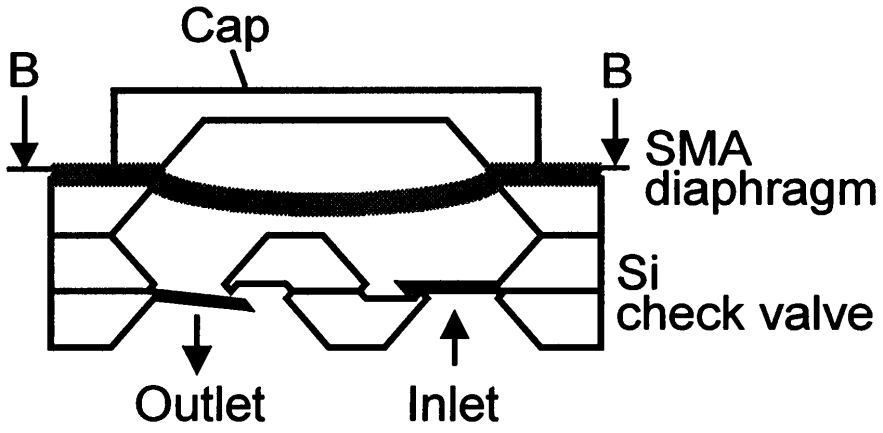

Figure 4: A diagram of a typical micropump using a shape memory alloy as an actuating diaphragm and inlet and outlet valves to control flow.[7]

1.5 Shape Memory Alloys and Pseudo-Elasticity

Shape memory alloys show great potential in many applications due to their ability to deform large amounts and recover without any permanent deformation. This combined with their ability to repeat this through millions of cycles makes them ideal for use in actuation applications.[10] Shape memory occurs when a material is deformed and will return to its original shape upon heating the material. Pseudo-elasticity occurs when

the material is deformed and returns to its original shape once the load is removed (Figure 5). Both these phenomena usually occur within the same alloy systems and the temperature at which the phase change occurs dictates which property the material has.[10] There is a low temperature, highly ductile phase martensite and a higher temperature phase austenite and where this phase change occurs relative to the environment in which the material is placed will determine if it is shape memory or pseudo-elastic.[9,10] The transformation temperatures at which the phase begins and ends are important when discussing shape memory alloys and both the martensite and austenite phases have a start and a finish temperature. When heating the material from martensite to austenite, the transition temperature at which the transformation occurs is called the austenite start (A_s) temperature and when the transition is complete its called the austenite finish (A_f) temperature. When cooling from austenite to martensite, the transition temperature at which martensite begins to form is called the martensite start (M_s) temperature and when the transformation ends it's called the martensite finish (M_f) temperature. Composition, grain size, processing, heat treatments and loading conditions can greatly alter the shape memory properties.[10] This can either be a disadvantage when attempting to control for all of these and achieve a constant result or it can be an advantage where it only takes small changes to greatly change the properties.

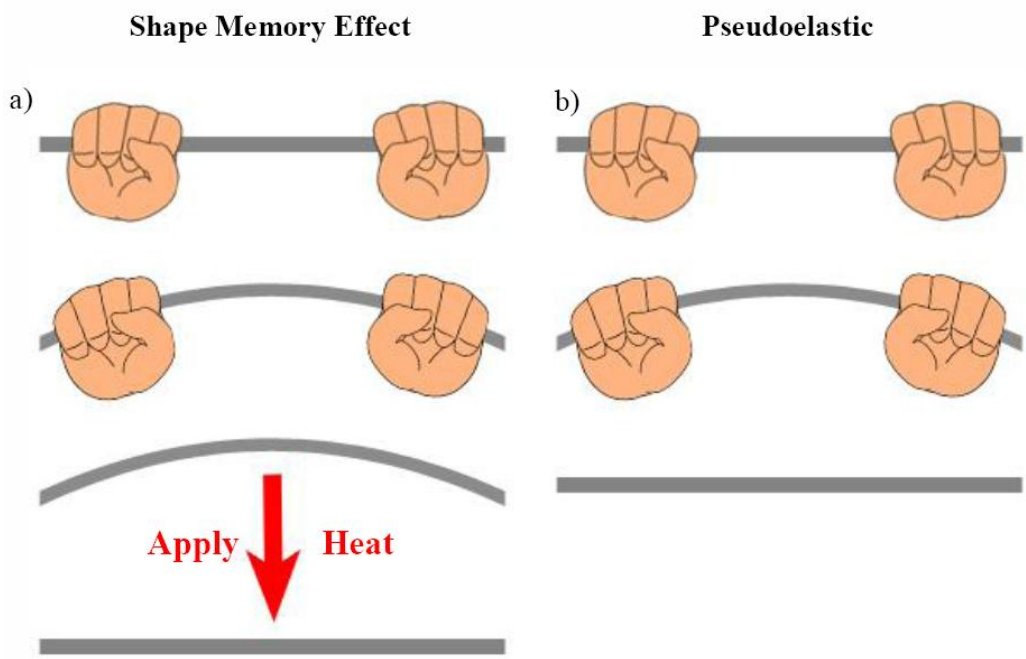

Figure 5: Diagram showing a) shape memory effect versus b) pseudoelastic (superelastic).[11]

The reason the deformation is recoverable due to the difference in plastic deformation mechanism between traditional metals and shape memory alloys. Traditional metals deform through dislocation motion while shape memory alloys begin deformation by preferential alignment of twins within the martensite structure (Figure 6).[9] Deformation caused by dislocation motion is not recoverable due to the extent of planes of atoms moving within the crystalline structure. Twinning and detwinning is easily recovered since no atomic bonds are broken nor created as opposed to the breaking and reforming of atomic bonds found during dislocation motion. Once all the twins become aligned, dislocation motion occurs and this deformation is not recoverable. The three most common crystalline shape memory alloys are NiTi, CuZnAl, and CuAlNi.[10]

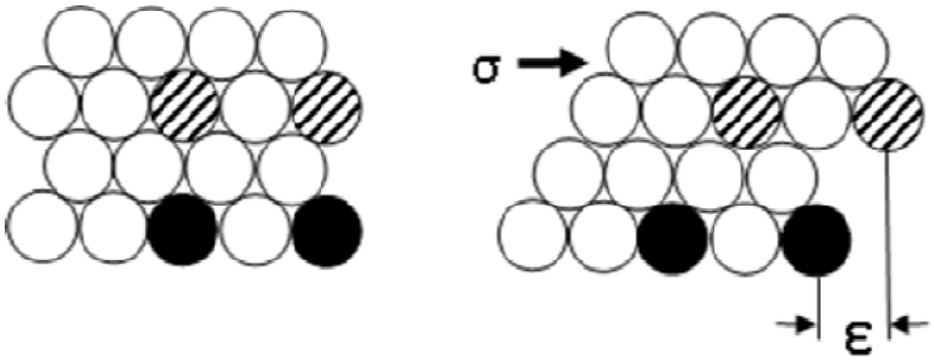

Figure 6: Dislocation motion found in traditional metals.[12]

NiTi is the most common shape memory alloy chosen for MEMS applications. This is due to all of the following: the low cost and highly reliable deposition techniques, reliable and precise characterization of the shape memory properties, variety of heat treatments, precise etching and patterning, and abundance of prediction models available for design and simulation of the non-linear behavior of shape memory alloys.[13] NiTi is also highly biocompatible due to the titanium oxide that forms on the surface of the material which forms a passivation layer protecting the body from the material.[14] The TiO_2 layer is also favored over other titanium and nickel oxides.[14] The oxide layer increases the stability of the surface layers by preventing further corrosion and creates a physical and chemical barrier against nickel oxidation.[14] NiTi also has a high work function in relation to the other shape memory alloys, which means it is able to exert large forces when transforming from martensite to austenite.[15]

1.6 Nickel-Titanium Shape Memory Alloy

Buehler et al. first discovered NiTi shape memory alloys in 1963.[16] The alloy was difficult to process, expensive to produce and was a highly complex phase system which

researchers didn't fully understand until the late 1980's.[17] But recently the growth in the use of NiTi for medical applications has exploded due to the increasing demand of minimally invasive medical procedures.[18] The uses of NiTi in medical applications range from endoscopic instruments, stents, filters, and orthopedic devices all due to the shape-memory and superelastic properties combined with high biocompatibility.[18] Like other shape memory alloys, the shape memory and superelastic properties rise from the diffusionless phase transformation that occurs between the high temperature austenite phase and the low temperature martensite phase.[18] The temperature at which this transformation occurs (A_f) varies and can be altered with different heat treatments. NiTi is an intermetallic that occurs at a 50:50 atomic composition and any deviation from that will move the composition into a two-phase region in the phase diagram (Figure 7).[18] Ni-rich NiTi is able to easily be heat treated due to some solubility, but this is not the case for Ti-rich NiTi which has no solubility as seen as the vertical line on the phase diagram.[17] Small amounts of impurities can also alter the transformation temperature as they react with the titanium and form precipitates which leads to Ni-enrichment.[18]

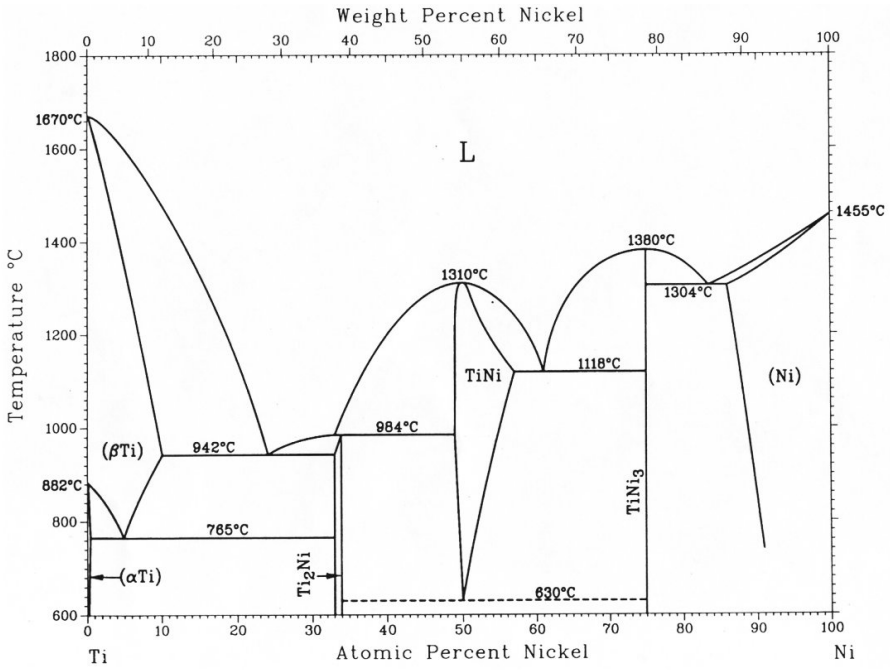

Figure 7: Phase diagram of nickel and titanium.[17]

The shape memory cycle consists of three main steps with many steps and phase changes occurring in between (Figure 8). The most important temperature to determine if the material is shape memory or pseudoelastic is the A_f temperature.[17] If the A_f temperature is above the environment temperature (in this case room temperature) the equilibrium phase will be twinned martensite. When a load is applied the twins move to accommodate the load; when the load is removed, the deformation remains. This new phase is called deformed martensite. Strains ranging from 6-8% are obtainable just from detwinning of the twinned martensite phase.[17] Further loading and deformation will result in dislocation motion and thus permanent and non-recoverable deformation. Heating the deformed martensite will transform it to austenite and cooling the material will result in the original twinned martensite phase.

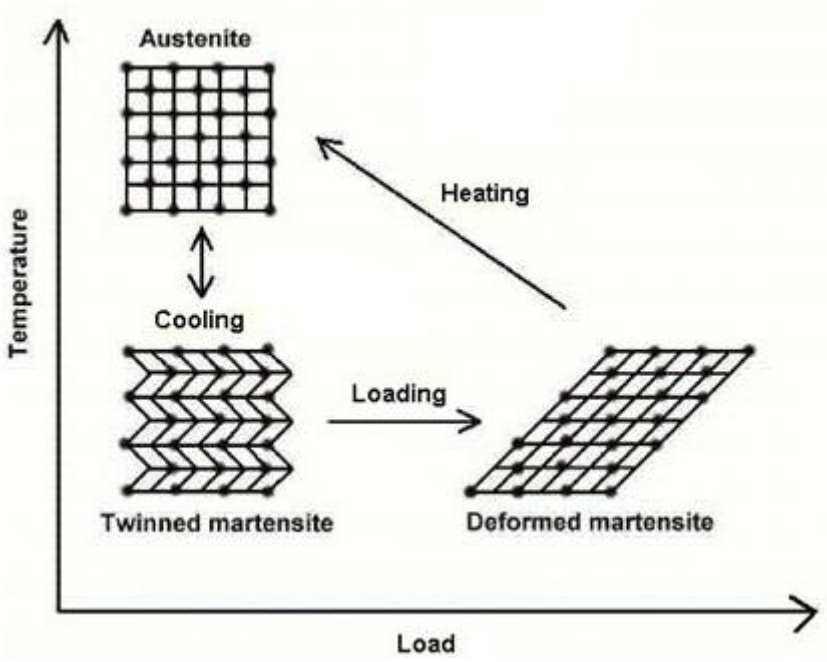

Figure 8: NiTi shape memory alloy cycle.

The martensitic transformation determines almost all of the important properties of shape memory alloys like the shape memory effect and pseudoelasticity.[17] When adding alloying elements, the transformation temperature greatly changes.[17] Alloying elements, Fe, Co and Pd prefer substituting for Ni while Mn, Cr and Cu tend to substitute for both Ni and Ti.[17] A variety of atom properties like electron configuration, chemical affinity and atomic size all play a role in site preference.[17] The effect of alloying elements on the martensitic transformation temperature is huge; a 1% by weight addition of an atom can increase the transformation temperature by more than 100°C.[17] Due to the ordered B2 crystalline structure of NiTi, there is an ability to dissolve excess Ni but not excess Ti.[17] Due to the inability to dissolve excess Ti in NiTi, Ti-rich NiTi is unobtainable in standard conditions and will act as an equiatomic Ni/Ti material. This changes when moving to thin-films since thin films are typically deposited in the

amorphous state and are needed to be annealed to create a crystalline structure that is either shape memory or pseudoelastic. When looking at Ni, the solubility allows for Ni-rich NiTi. The excess Ni in the NiTi ordered structure causes a change in the elastic constant of the structure which changes the ability to transform phases with an applied stress or applied heat.[17]

Heat treatments on equiatomic NiTi do not change anything within the structure or alter the transformation temperature.[17] Heat treatments on Ni-rich alloys occur due to the solubility of Ni in NiTi. This excess leads to the ability to form a supersaturated solid solution which then is able to be heat treated and aged to form Ni-rich precipitates which remove the excess Ni from the NiTi intermetallic.[17] This creates a metastable-equilibrium between the NiTi and the Ti_3Ni_4 intermetallic.

1.7 Thin-Film Nickel-Titanium Shape Memory Alloy

One weakness of shape memory alloy actuators is the slow response time, or the time it takes for the device to heat or cool.[19] This is overcome by the use of thin-films where the surface area to volume ratio is high. The relatively large surface area allows for a large amount of heat transfer to occur while the small volume allows for quick cooling and heating. Depositing NiTi in a thin-film has been researched and well characterized by many researchers, including previous work done at Cal Poly.[19] These films are typically RF or DC magnetron sputtered. If deposited onto a cool substrate the film will be amorphous and must be annealed to crystallize the film which is done above 500°C.[19] Silicon is a good choice for a substrate due to the high adhesion strength NiTi has with silicon.[11,12,19,20] If an insulation layer is required for ohmic heating, an adhesion layer is necessary due to the low adhesion strength between NiTi and silicon dioxide or silicon

nitride. [11,12,19,20] Chromium makes for a good adhesion layer due to the high adhesion strengths between chromium and NiTi and chromium and silicon dioxide as well as the ease of deposition through DC magnetron sputtering.[11,12,20] Once the material is deposited onto the proper substrate, it can be annealed. The annealing step crystallizes the material and does initiate the precipitation process which determines the transformation temperature. Both the crystallization and precipitation steps occur simultaneously. A transformation temperature above room temperature (or operating temperature) is needed, but it must not be much higher since more power to heat the NiTi will be needed.[19]

1.8 Processing of Thin-Film NiTi SMA

As stated before, thin-film NiTi has the ability to act differently than bulk NiTi. This is due to the deposition techniques used to put down NiTi in a thin-film form. There are a variety of techniques used to deposit NiTi. The two most common are both physical vapor deposition (PVD) processes: sputtering and flash evaporation. Evaporation involves heating a crucible which holds the target material within a chamber with a high vacuum. The crucible is heated with high amounts of current and the target material boils and evaporates the target material which then is able to condense onto the substrate.

Sputtering employs a plasma to ionize argon atoms which then collide with a target material which is then deposited onto the substrate (Figure 9). Both DC and RF sputtering can be utilized to sputter NiTi, but this work will use DC due to the abundance of previous research characterizing the sputtering process. A DC power supply creates a charge on the cathodes with negative voltages. The negative voltage repels free electrons in the plasma away from the cathode. Rare earth magnets shaped in a ring placed below the sputtering target force the electrons to spiral obey the magnetic lines of force which

increases the chances of a collision to happen with an Ar atom. These collisions remove outer shell electrons which leads to an ionization of the Ar atoms. This process creates a high energy plasma. The negative cathode is then bombarded with the positively ionized Ar atoms which then causes the target material to eject neutral atoms off the surface of the target. Due the large size of Ar, it is able to eject many atoms per Ar atom collision. These ejected target atoms then deposit and adhere to the substrate which creates an amorphous thin film. Co-sputtering was used in this work due to the difference in sputter rates between Ni and Ti. Ti has a much lower sputtering rate and therefore an extra target of Ti is needed to balance and create near equiatomic NiTi.[21] Elemental composition can easily measured using a variety of techniques like energy dispersive spectroscopy and x-ray florescence.

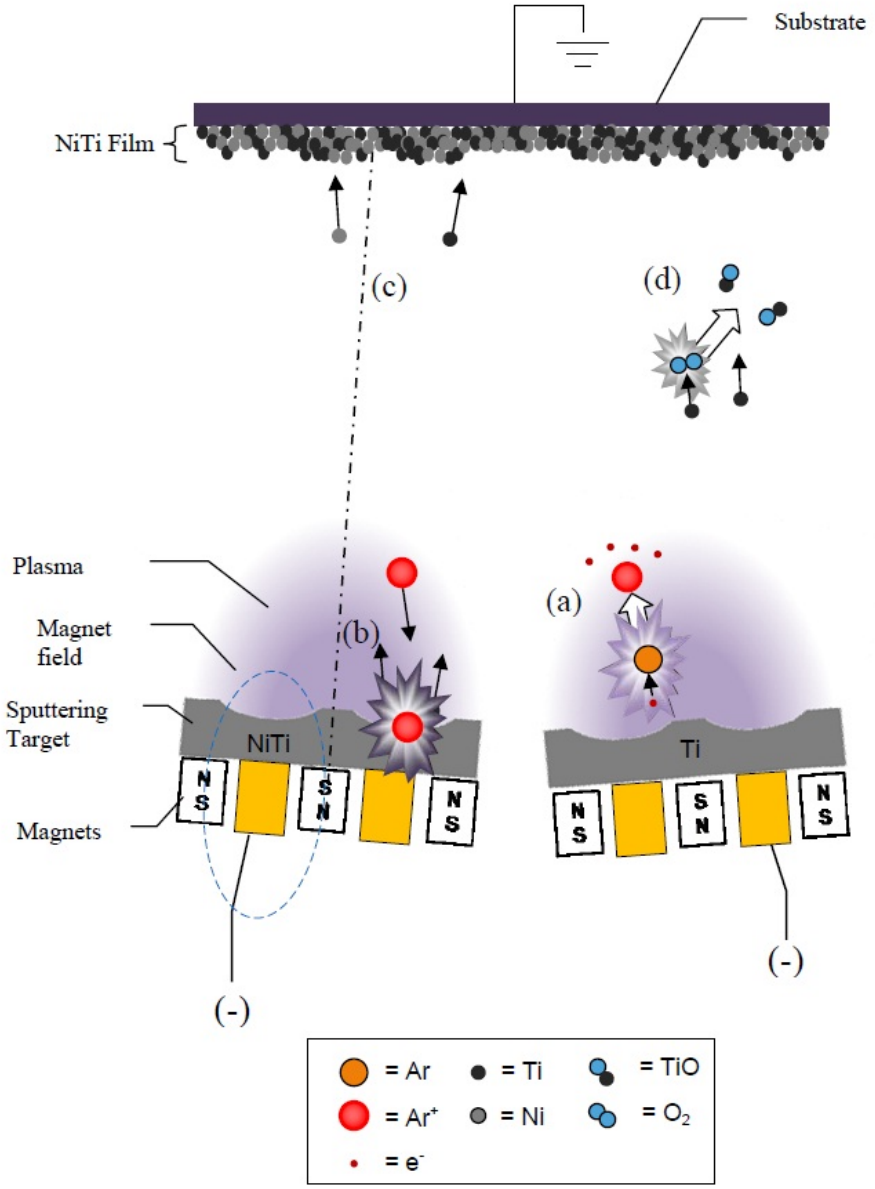

Figure 9: DC magnetron sputtering process: a) argon ionization, b) target ejection, c) deposition, and d) thermalisation.[12]

As stated before, sputtering yields an amorphous film that needs to be annealed in order to crystallize and create the NiTi intermetallic. Research has shown that sputtering NiTi onto a glass, quartz or silicon that is below 200°C will give an amorphous film.[17] Due to annealing process which is non-equilibrium process, Ti-rich and Ni-rich NiTi are

obtainable.[17] Both these structures yield different microstructures and careful attention must be paid to obtain a desirable film. Small changes in pressure, target and substrate temperature, target composition and time could all lead to drastic changes in film composition. In general, transformation temperatures of near-equiatomic and Ti-rich films are above room temperature while Ni-rich films are below.[22] Ni-rich films tend to follow similar processes and properties as the bulk Ni-rich NiTi.[17] While the Ni-rich films tend to have Ti_3Ni_4 precipitates, the Ti-rich films tend to form Ti_2Ni precipitates.[17] Ti-rich films retain the shape memory characteristics with recoverable strains up to 5.5%.[17] Research has also shown that Ni-rich and equiatomic films crystallize at a much higher and constant rate than Ti-rich films.[23] Heat treatments at the lowest temperature are desired due to a reduced chance of reactions with the substrate material, which in most cases is silicon.

Nucleation and growth phenomena determine how the NiTi thin-film crystallizes during heat treatment. It is known that high heat treatments lead to high amounts of nucleation and therefore much finer grains are obtained. Heat treating at a lower temperature leads to less nucleation and more growth leading to much larger and coarse grains. This has been observed research and seems to apply directly to thin-film NiTi.[23] Grain size has not been shown to affect the A_f temperature directly.

Substrate material choice can be an important variable when sputtering thin films. Research has shown that sputtering on silicon and silicon dioxide (grown thermally) yields similar crystalline structure and shape memory properties after heat treatment.[24] It was found that an oxide layer acts as a diffusion barrier decreasing the size of the diffusion zone between NiTi and Si/SiO_2.[24] The disadvantage of sputtering onto oxide is

the poor adhesion which has been reported in a variety of works.[11,12,20,24] But this oxidation can easily be prevented by sputtering another material to act as a diffusion barrier for oxygen like chromium. This layer will prevent the NiTi from being oxidized and be easily removeable in later steps during processing. Stress-strain measurements on films sputtered onto Si and SiO_2 have shown similar results.[25]

Sputtering NiTi from a NiTi target does not yield the target composition in the film; Ti has a higher sputtering resistance than Ni.[21] Sputtering yield analyses on sputtering with Ni and Ti targets versus NiTi and Ti targets show that the NiTi/Ti yield superior results due to the problem of sputtering rings in the targets (Figure 10).[21] These grooves alter the vapor flux from the target.[21]

Figure 10: Picture of a NiTi and a chromium target after magnetron sputtering showing the rings in the target after a few sputtering cycles.

Chapter 2 - Project Overview

2.1 Long Term Scope

The long term scope of this project is to create a functioning micropump for use in microfluidic devices created here at Cal Poly. Currently large external syringe pumps are used to push liquids through our microfluidic chips; these syringe pumps are much larger than the chips and the connection between the syringe pumps and the chips are inconsistent and difficult to create without leaks. An internal pumping system is needed to be able to pump liquids through our microfluidic chips that is both small in size, to match the size of the chip, and can easily be connected and interfaced. The syringe pumps offer a high amount of control of the flow rates and head pressures, but that is the only advantage of them currently.

Another long term scope of this project is to create a pump that is able to apply various pressures into a sealed chamber with a variable focus PDMS lens. Currently there is work being conducted on characterizing and optimizing the process and design of the PDMS variable focus lens, but to apply the pressure to the chamber a large syringe is being used. The syringe, like the syringe pump, is much larger than the actual device and a device of the same size scale is desired to apply the pressure to the lens. The advantage of the NiTi diaphragm is that different pressures could be easily obtained by just slight changes in temperature. The heat could easily be created with ohmic heating with an applied current. So by adjusting the current different pressures could be obtained and therefore different focal lengths in the PDMS lens.

2.2 Previous Work

Previous NiTi thin film work has been conducted by multiple individuals (E-G).[11,12,20] Thin film NiTi has been deposited onto silicon substrates and characterized with differential scanning calorimetry (DSC), energy dispersive spectroscopy (EDS), x-ray florescence (XRF), and atomic force microscopy (AFM). Near equiatomic percent NiTi can be deposited using a dual-cathode magnetron sputtering system with a NiTi and Ti target. By varying the power to each target near equiatomic NiTi mix can be obtained. This film can then be heat treated in a vacuum furnace crystallizing the amorphous as-sputtered film and then heat treating the NiTi to make it shape memory. Simple cantilever devices have been fabricated, but due to the high amount of stresses introduced during the sputtering process, functioning devices have been difficult to create with any sort of consistently.

2.3 Scope of Current Work

This project was more focused on being able to develop a process in which a functioning NiTi device could be made and characterized. The recipe and process to sputter NiTi have already been well characterized by previous work. Also, the deep silicon etching process has been well characterized by work done by Brian Stahl.[26] All other processes used in this work have also been well characterized by many individuals.[11,12,20,26] Various processes needed to be combined in order for this project to succeed and further characterization of the processing steps was done. In addition to creating the device, quantification of the performance of the diaphragm was conducted in

order to see the amount of deflection and percent recovery and compare this to theoretical models published for these types of thin-film membranes.

Chapter 3 - Processing

3.1 Process Overview

There were many steps in creating the thin-film NiTi diaphragm; each was carefully characterized to ensure that replications could be made and that consistent results could be achieved (Figure 11). In short, a thermal oxide was grown upon a silicon wafer and the oxide was patterned on one side using positive photolithography. The backside was coated with positive photoresist to protect the oxide. The oxide was then etched and the photoresist stripped. This wafer was then deep etched in a 25% by weight of tetramethylammonium hydroxide (TMAH) to etch the silicon leaving only a thin membrane. The oxide was then etched off and NiTi was DC magnetron sputtered onto the flat side of the wafer followed by chromium. The NiTi thickness was measured to be around 5 μm and the Cr layer was 500 nm. The wafer was then annealed in a vacuum chamber at 550°C for 1 hour to crystallize and shape set the NiTi. The wafer was then dry etched in a reactive ion etcher to etch away the remaining silicon. The chromium was then etched off using a chromium etchant.

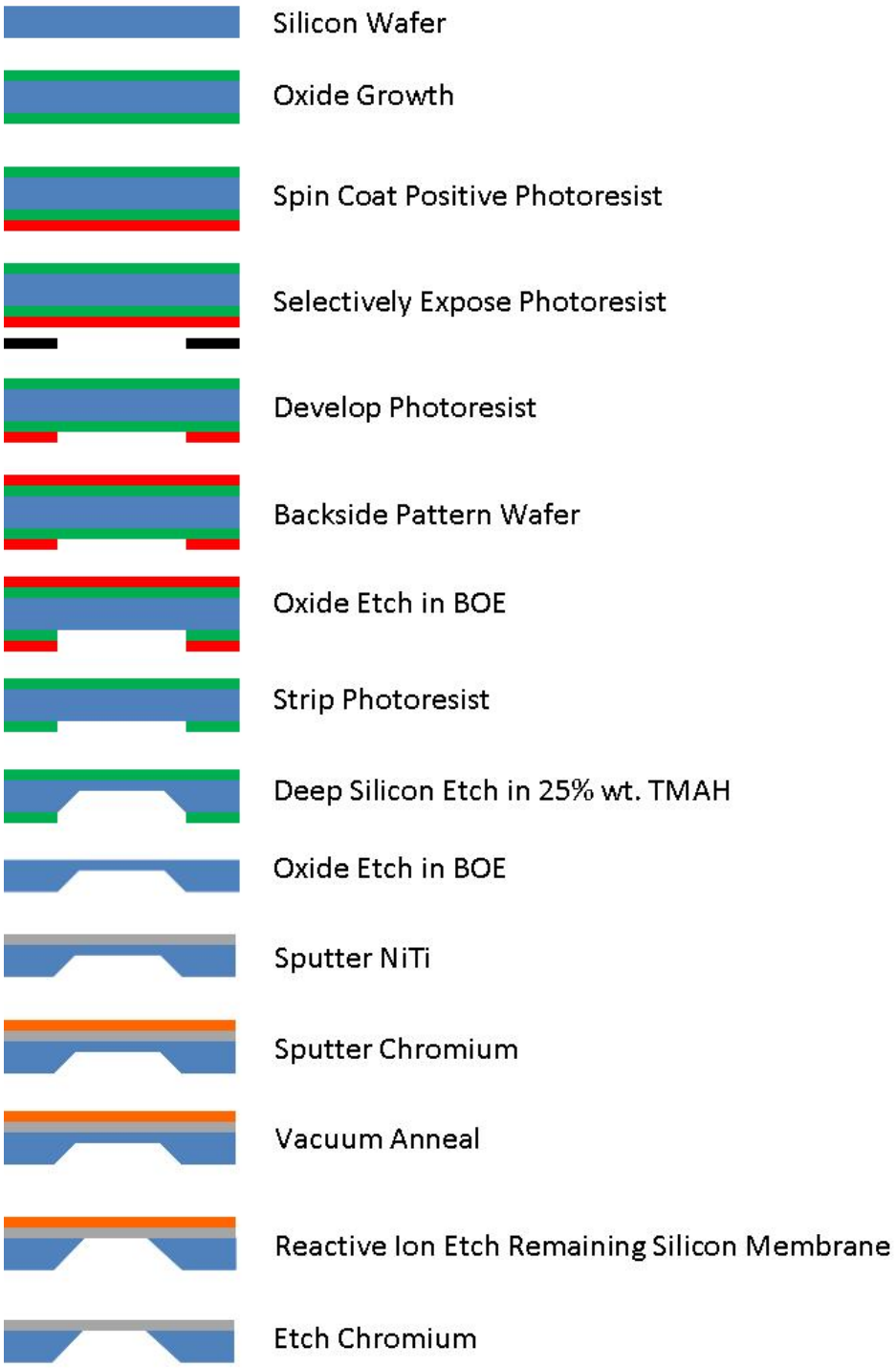

Figure 11: Process overview and cross-sectional view of the creation the thin-film shape memory alloy diaphragm.

3.2 Wafer Choice and Cleaning

Processing was conducted using only equipment available in Cal Poly's Class-1000 Microfabrication Lab (building 41-203). Processing began with a silicon wafer substrate. The wafers were 100 mm diameter, N-type doped with phosphorous to a 10-20 ohm-cm resistivity, <1-0-0> orientation, 400 μm thick, double-sided polished silicon wafers. These wafers were selected due to the large quantity of extras from previous projects. Any double-sided polished wafer would work, but a thickness no greater than 400 μm was desired due to the inability to measure etch depth past 400 μm. P-type wafers could easily be substituted yielding similar results in every step, but would lead to a much easier ability to anodically bond to glass slides.

The process started with the wafers placed in piranha at 70°C for 10 minutes. Piranha is a 9:1 ratio of sulfuric acid to hydrogen peroxide which etches away any organics that might be on the silicon surface. The wafers were then rinsed with deionized water and placed in buffered oxide etchant (BOE) which will remove any native oxide found on the wafers. After the DI water rinse, the wafers are dried with low purity (99.99%) nitrogen gas. Once these cleaning steps are completed, the oxide can be grown that will act as the mask for the silicon etching step.

3.3 Thermal Oxide Growth

An oxide mask was chosen for the silicon etching step due to the ease of oxide growth and masking with positive photolithography. Also, previous work has shown the high selectivity of silicon over oxide with the TMAH silicon etchant used.[26] It was found that the selectivity of silicon to oxide was over 6000:1.[26]

The wafers are placed in a quartz boat that is able to withstand the high temperatures needed for oxidation. Dummy wafers were placed at the ends of the boat to create a more uniform flow of gases that will more evenly grow the oxide over the silicon wafers (Figure 12). Oxide growth is done in a Thermco tube furnace (Figure 13). The process followed as stated in the SOP. The furnace is then turned on and heated to about 900°C. At this point, dry ultra high purity (99.999%) nitrogen gas is flowed into the chamber at around 5 L/min and the cap of the furnace is removed. The gas is used to prevent the growth of an oxide at a lower temperature than desired.

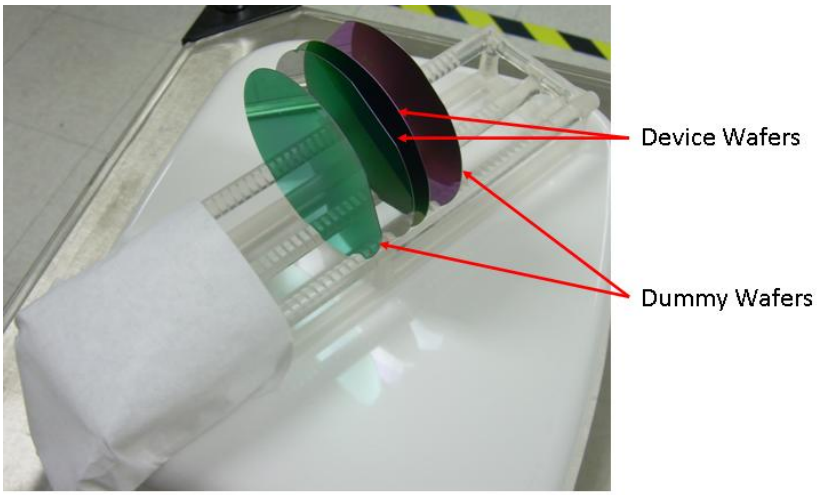

Figure 12: Picture showing the quartz boat used for thermal oxides with the device wafers in the middle surrounded by dummy wafers.

Figure 13: Picture of the thermal oxide and diffusion tube furnaces. The top tube is only for thermal oxidation processes and the bottom is only for diffusion processes.

The quartz boat is placed inside and the cap is placed back on. Using a glass rod, the quartz boat is pushed toward the center of the furnace at a rate less than0.5 cm/s to prevent thermal shock in the silicon wafers. The furnace is then turned up to the desired temperature, in this case 1100°C was chosen to reduce the amount of time the furnace needs to run. Also, the deionized water heater must be turned on to ensure the water is 100°C when the furnace reaches temperature. Using a Deal-Grove model, the furnace calibrations, and the desired oxide thickness, the time to grow that oxide can be estimated. For 1100°C and a desired thickness of 500 nm, the wafers must be in the furnace for about 90 minutes.

There are two different types of oxide able to be grown: dry and wet. Dry oxide is grown by flowing oxygen gas into the chamber. This leads to a dense, low thermal conductivity and high electrical resistivity oxide layer, but grows at a slow rate.[27] Wet oxide is grown by flowing oxygen gas through boiling water which leads to a less dense, more conductive oxide layer that grows much more quickly.[27] The reason for the faster oxide growth is due to the diffusion constant and solubility of O_2 gas versus H_2O gas. Water has a much higher solubility and diffusion constant over oxygen gas since it is a much smaller molecule.[27] Since the oxide is going to be a mask for the silicon etching, a wet oxide is enough and the higher growth rate makes it more desirable.

Once the temperature reaches 1100°C the high purity nitrogen gas is shut off while the ultra high purity (99.994%) oxygen is turned on with the option of "wet" selected and a flow rate of 5 L/min. The wafers are then left to grow the oxide for the desired time. Once the time is done, the oxygen gas is shut off as well as the furnace while dry nitrogen gas is turned back on. The water heater is also shut off. The furnace will begin to slowly cool and the nitrogen gas will again prevent oxide from growing at a lower temperature than desired. Once the furnace reaches about 900°C, the nitrogen gas can be shut off since the oxide growth at 900°C and below is negligible compared to 1100°C.

The oxide thickness was confirmed and recorded using the Filmetrics relectometer tool (Figure 14). The Filmetrics tool was used following the SOP found in the cleanroom. The lamp was turned on and allowed to warm-up for about 30 minutes. The Filmeasure program on the computer adjacent to the tool was turned on and the option of a SiO_2 layer on Si was chosen. A reference bare silicon wafer was placed in the

light and a background spectrum was taken. The wafer was removed for the dark spectrum. A reference SiO_2 wafer was used to confirm the accuracy of the tool. The tool was found to constantly be within 5% of the actual value of the reference oxide layer, which is more than enough for this project. The device wafer was then placed under the lamp and five measurements were taken at random points around the wafer; the edges and center were common points to measure to as the center was typically thicker than the edges. The values were then be recorded and compared to the values expected from the Deal-Grove Model.

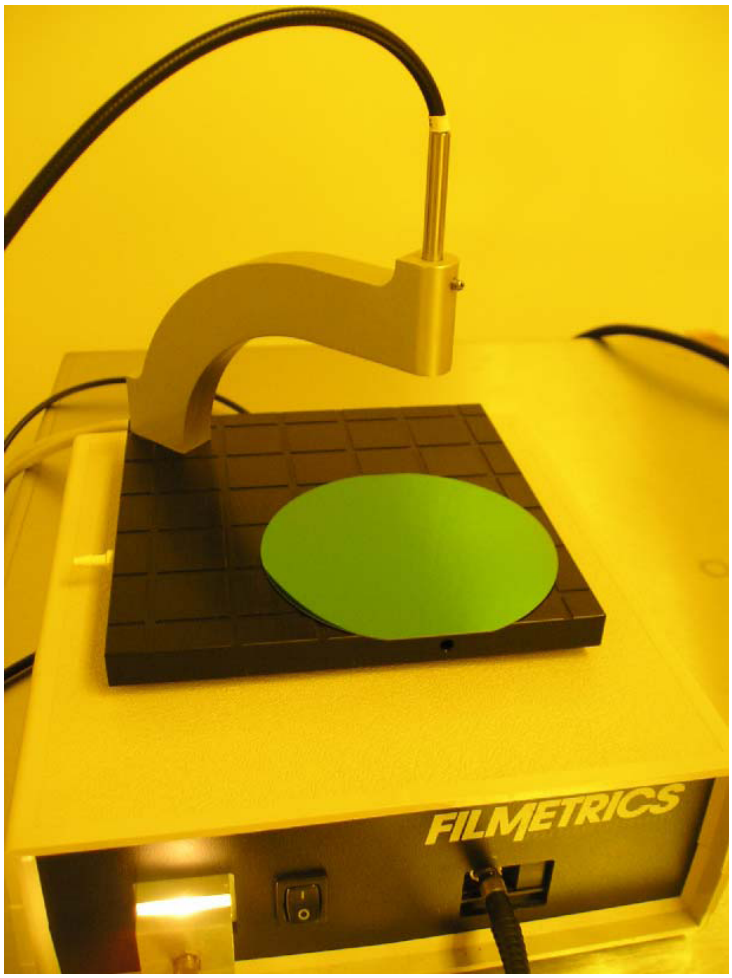

Figure 14: Filmetrics reflectometer tool.

3.4 Positive Lithography

Once the oxide is grown, it needs to be masked with the square membrane shape. This is done using positive lithography which includes spin coating a photoactive polymer onto the wafers, selectively exposing the polymer to ultraviolet light, developing the soluble polymer, and hard baking the remaining polymer. This polymer mask can then be used to selectively etch the oxide below.

3.4.1 Spin Coating

The first step to the lithography process is to spin coat the photoactive polymer. The wafer is placed in the spin coater (Laurell Technologies Corporation WS-400 B-6N PP / Lite / AS) and the vacuum pump is turned on. The surface is then prepared to ensure a good adhesion between the oxide and the polymer. This is done using a primer that turns the surface from hydrophilic to hydrophobic. This is desired since the polymer is dissolved in a hydrocarbon-based solvent. The primer used is MCC Primer 80/20 from MicroChem. About 3 mL is poured onto the wafer and the first two steps of spin coaters program runs (Table II). Once the first two steps are done, about 3 mL of Shipley S1813 photoresist is poured onto the wafer. The rest of the steps are run in the spin coater.

Table II: Spin coating steps used for Shipley S1813 positive photoresist.

Step #	Time (s)	Speed (rpm)
Pour 3 mL of MCC Primer 80/20		
1	30	300
2	20	3000
Pour 3 mL of Shipley S1813 Photoresist		
3	20	200
4	10	1000
5	20	4000
6	5	300

The vacuum is removed and the wafer is then placed onto a hotplate which is at 90°C for 1 minute. This soft bake process removed excess solvent before the exposing process. The wafer is then placed on a chilled plate to cool back down to room temperature.

3.4.2 Mask and Alignment

Once the wafer with the photoresist is soft baked, it was moved to the exposure process with the aligner. Microposit recommends a 150 mJ/cm^2 dose while the Canon Parallel Light Mask Aligner with its mercury vapor arc lamp puts out 6.5 mW/cm^2; this means the optimum exposure time is 23 seconds. The aligner runs with a light integral which a 1.0 leads to about 3.7122 second exposure; this leads to a light integral of about 6.2. The areas exposed to the UV light become soluble and dissolve in the developer while the unexposed areas remain the same. The mask used was created for an electrostatic silicon membrane project by Brian Stahl, but the mask was easily still used for this project (Figure 15). The five different sized membranes were as follows: 1294 μm, 2194 μm, 2994 μm, 3694 μm, 4394 μm.

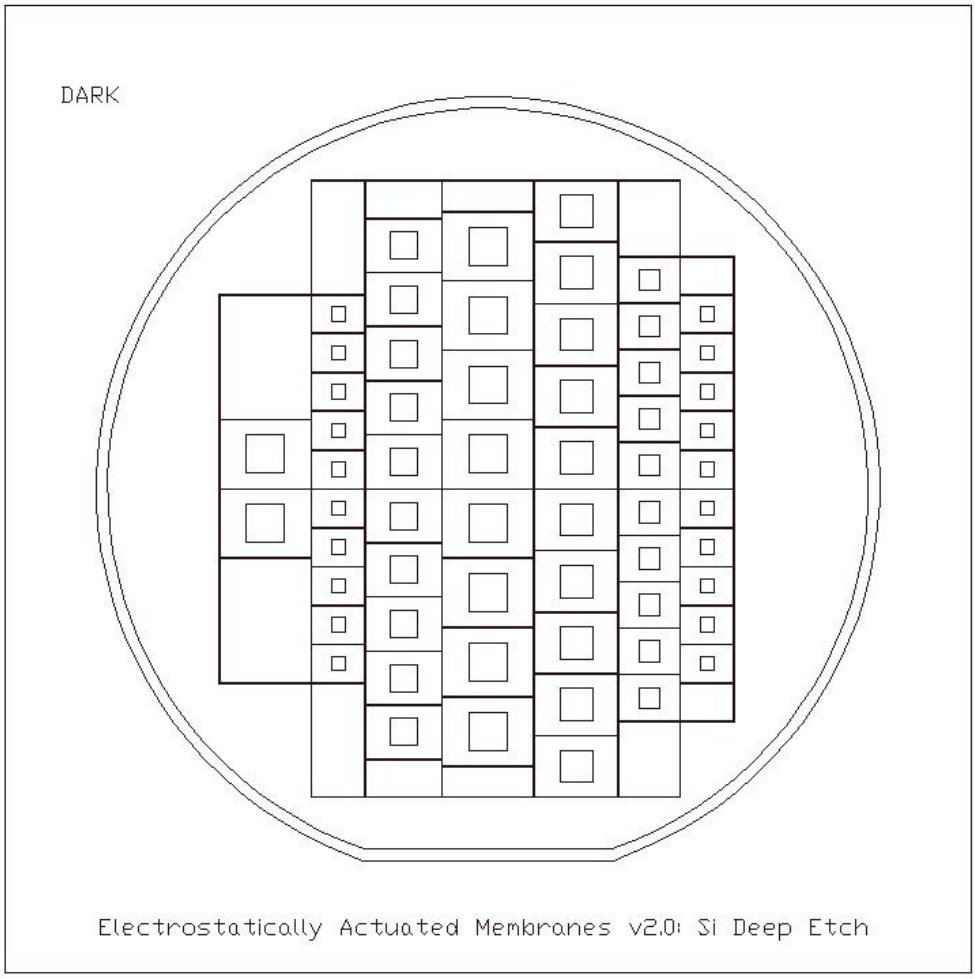

Figure 15: Diagram of mask used to selectively expose the positive photoresist to create the oxide mask for the deep silicon etching step. The squares will become the etch pits and the region around the squares will be the supporting silicon.

3.4.3 Developing

Once the exposure step is completed, the soluble, exposed photoresist needs to be dissolved away. The developer used for this step is Microposit MF CD-26 Developer. This metal-free developer is for high resolution immersion developing which is necessary for semiconductor processing. The wafer is placed in this solution for about 4 minutes with slight agitation. After the allotted time, the wafer is taken out and cleaned with DI

water. The wafer is then dried with low purity nitrogen gas. The wafer is then hard baked to ensure all the solvent is removed and the polymer is fully cured.

3.4.4 Backside Patterning

Once one side has the oxide masked, the other side must be coated as well. There is no exposure or developing step here since this side is not to be masked and simply acts to protect the backside oxide. During the silicon etching step, only the masked pits are desired to be etched and the backside must be protected to ensure further processing with the wafer. The same steps are followed, only omitting the exposure and developing steps.

3.4.5 Selective Oxide Etch

The oxide is etched away since the adhesion between NiTi and oxide is negligible.[11,12,20,24] The oxide is masked on one side and protected on the other, so the oxide must now be selectively etched with the photoresist protecting the rest. The wafer is placed in BOE for about 5 minutes and 30 seconds. The etch rate was confirmed to match previous works, which is around 100 nm/minute. The etch rate was measured by step etching a wafer with an oxide and no protective photoresist. The wafer was etched for 1 minute then moved further into the etchant creating five regions of different etch times. With a 500 nm oxide, 5 minutes of etching is required with 10% extra time to ensure all the exposed oxide is etched.

3.4.6 Stripping

With the oxide selectively etched, the oxide mask is complete and the photoresist must be stripped away since it is not able to withstand the silicon etchant. The stripping

process is done with Microposit Remover 1165 which corresponds to the S1813 positive photoresist. The wafers are dipped in the stripper for 5 minutes at 60°C with slight agitation. The wafers are then rinsed with DI water and dried with low purity nitrogen gas. The wafers are now coated with oxide with selective areas of silicon exposed. The wafers are now ready for silicon etching (Figure 16).

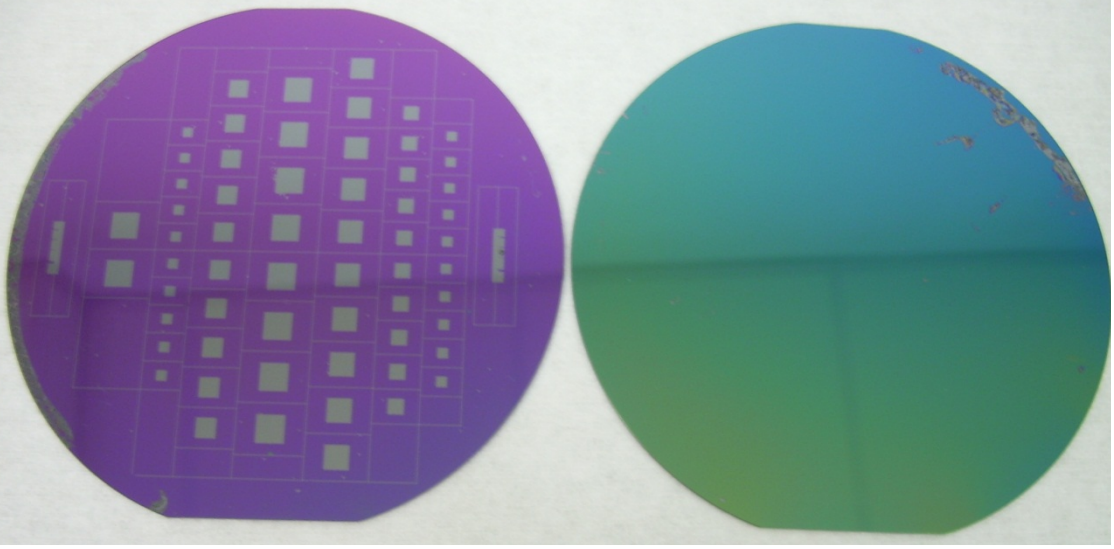

Figure 16: Picture a fully masked oxide ready for silicon etching. The colored regions are the remaining oxide while the shiny silver regions are the exposed silicon. The etch pits are clearly shown in the left wafer while the backside shows little to no exposed silicon in the right wafer.

3.5 Deep Silicon Etching

Due to the monocrystallinity of the silicon wafers, anisotropic etching can be used to etch silicon with distinct and predictable patterns. The two methods of etching silicon are dry and wet etching; dry etching usually is done with reactive ion etching or plasma etching while wet etching is done in an aqueous solution. Wet etching was chosen due to

the lower cost solutions of acidic or alkaline solutions. Previous work has characterized deep silicon etching with a variety of different etchants.[12,20,26] David Getchel worked with ethylenediamine pyrocatechol (EDP) as an anisotropic etchant but it was found to be too dangerous due to the highly corrosive nature, flammability, and carcinogenic nature of the etchant. Brian Stahl and Dustin Dequine worked with both potassium hydroxide (KOH) and tetramethylammonium hydroxide (TMAH, $(CH_3)_4NOH$). KOH was found to yield a weak selectivity of SiO_2 to silicon (less than 500:1) while TMAH yielded a selectivity of over 6000:1 (H). TMAH is also less toxic and can be purchased in ready-to-use formulations.

The etching mechanism for silicon in alkaline solutions is as follows[28]: surface silicon atoms react with the hydroxyl groups causing oxidation and four electrons to be injected into the conduction band of the silicon.

$$Si + 2(OH^-) \rightarrow Si(OH)_2^{2+} + 4e^-$$

The four free electrons reduce water in the solution, evolving hydrogen gas and creating four new hydroxyl groups.

$$4e^- + 4H_2O \rightarrow 4(OH^-) + 2H_2$$

The silicon compound Si(OH)2 reacts with four additional hydroxyl groups resulting in the formation of water and a water-soluble silicon compound.

$$Si(OH)_2^{2+} + 4(OH^-) \rightarrow SiO_2(OH)_2^{2-} + 2H_2O$$

The overall reaction is:

$$Si + 2(OH^-) + 2H_2O \rightarrow SiO_2(OH)_2^{2-} + 2H_2$$

The solution of TMAH used for this work was a 25% by weight aqueous TMAH. The solution was bought from Transene and poured directly into the condenser chamber

used solely for deep silicon etching (Figure 17). The hotplate was first turned on to a setting of 130°C and the stir rod speed setting of 2. The hot plate would heat the TMAH solution to about 70°C in about one hour. This was monitored with a thermocouple. After equilibrium was reached, the temperature controller was turned on and attached to the resistive heating wrap around the chamber. The thermocouple attached to the temperature controller was also dipped into the solution next to the other thermocouple through a condenser tube. The temperature controller setting was set to get the solution to 85°C. Once 85°C was reached, the chamber top was opened and a Teflon cassette with the wafer oxide mask facing up was slowly dipped into the solution. The top was then replaced and timer begun. Once the time is done, the temperature controller, hot plate and stir rod were all shut off and the thermocouples taken out and rinsed with DI water. The lid was then removed and the wafers removed from the solution carefully. The top was then replaced and the wafers carefully rinsed with DI water. At this point the wafers are extremely fragile and the utmost care in not breaking a wafer was required.

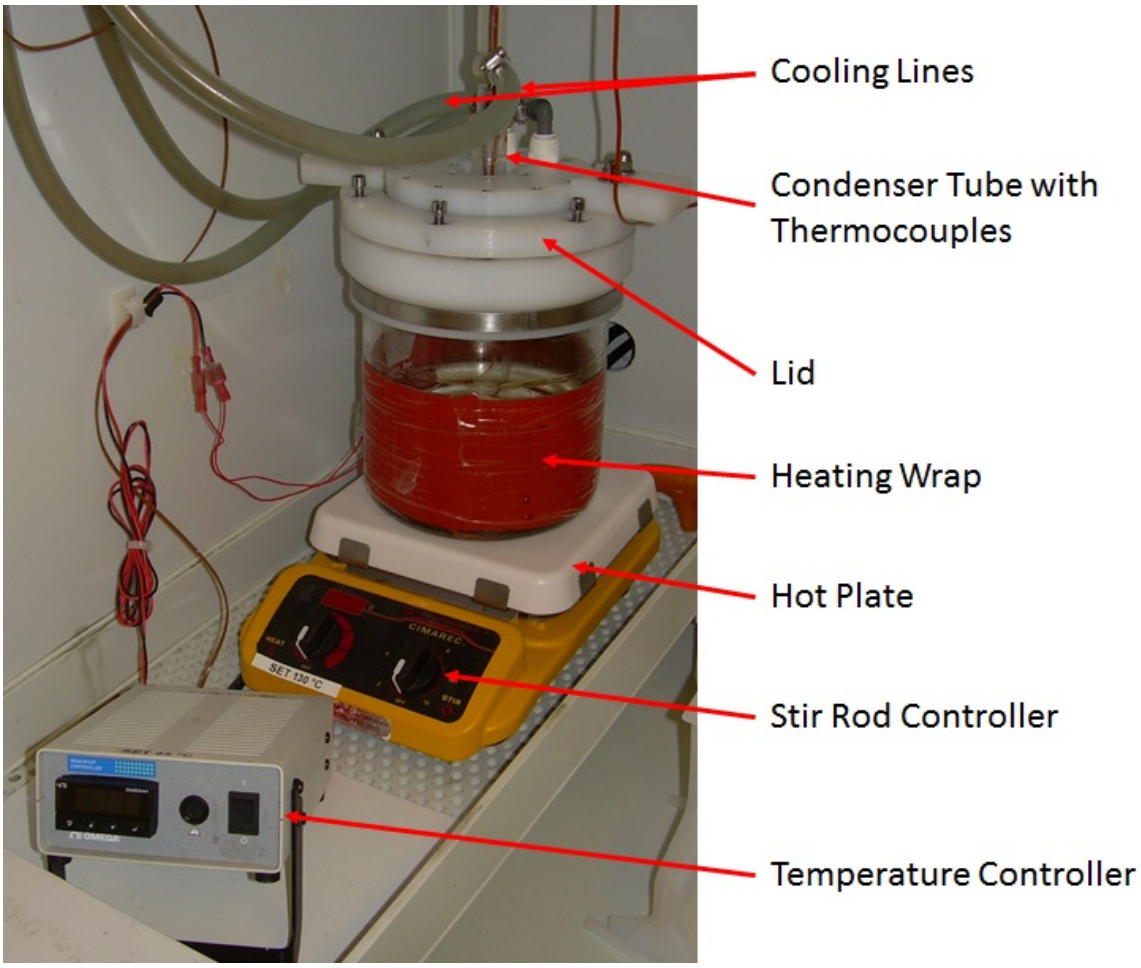

Figure 17: Picture showing the condenser chamber used for deep silicon etching along with the temperature controller.

The wafers were then measured to verify the thickness of the remaining silicon membranes. This was done using an Ambios Technology XP-1 profilometer. The profilometer uses a stylus which contacts the surface with an applied force (Figure 18). The profilometer then moves the stylus across the surface ensuring the applied force stays constant. If there is a change in elevation, the z-axis controller must move either up or down to keep the same load. This can then be carefully measured and plotted to obtain thickness data from a variety of processes from sputtering to etching to thin-film stress.

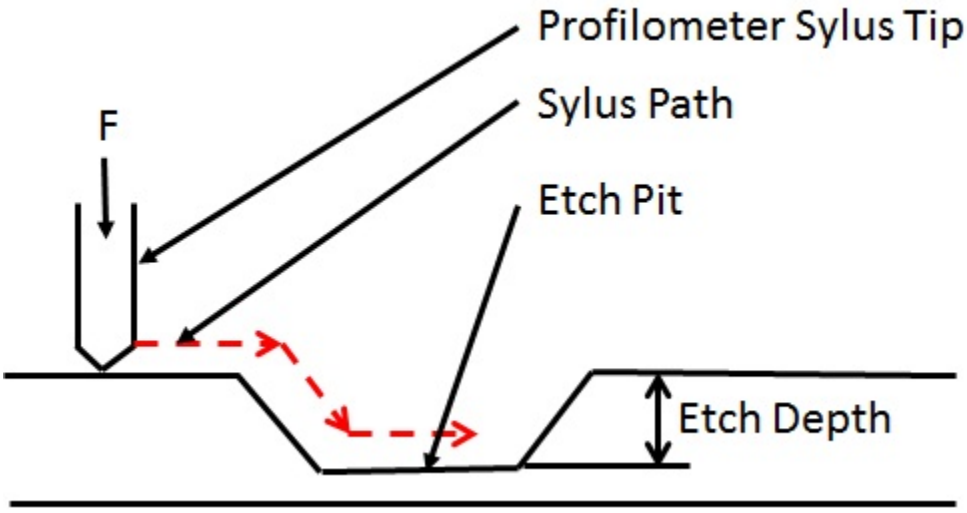

Figure 18: Diagram showing how the profilometer measures the etch pit.

The scans conducted were 0.05 mm/sec over a 1 mm scan length with a thickness range of 400 μm with a force of 1 mg. A variety of wafers were carefully measured at different increments of time to determine the etch rate. These values were recorded to obtain an etch rate. If the wafers were taken out prematurely and the silicon membrane thickness was too great, the wafers were simply placed back in the TMAH solution for more time. A silicon membrane thickness of 10 μm was desired to ensure minimum time etching it away later in the processing steps.

It was found that the etch rate greatly varied for the same parameters on wafers from the same batch (Figure 19, Table III). This is different than what was found in previous work at Cal Poly.[26] The large variation in etch rate between wafers was found to be the largest obstacle in all of the processing steps. It should be noted that the etch depth within a single wafer was highly uniform only having an average standard deviation of 0.96 μm between any single set of measurements within the wafer. Five measurements

were taken at random on each wafer for each etch time. The largest standard deviation within a single wafer was only 2.6 μm with an average etch depth of 313 μm; this occurred after 12 hours of etching.

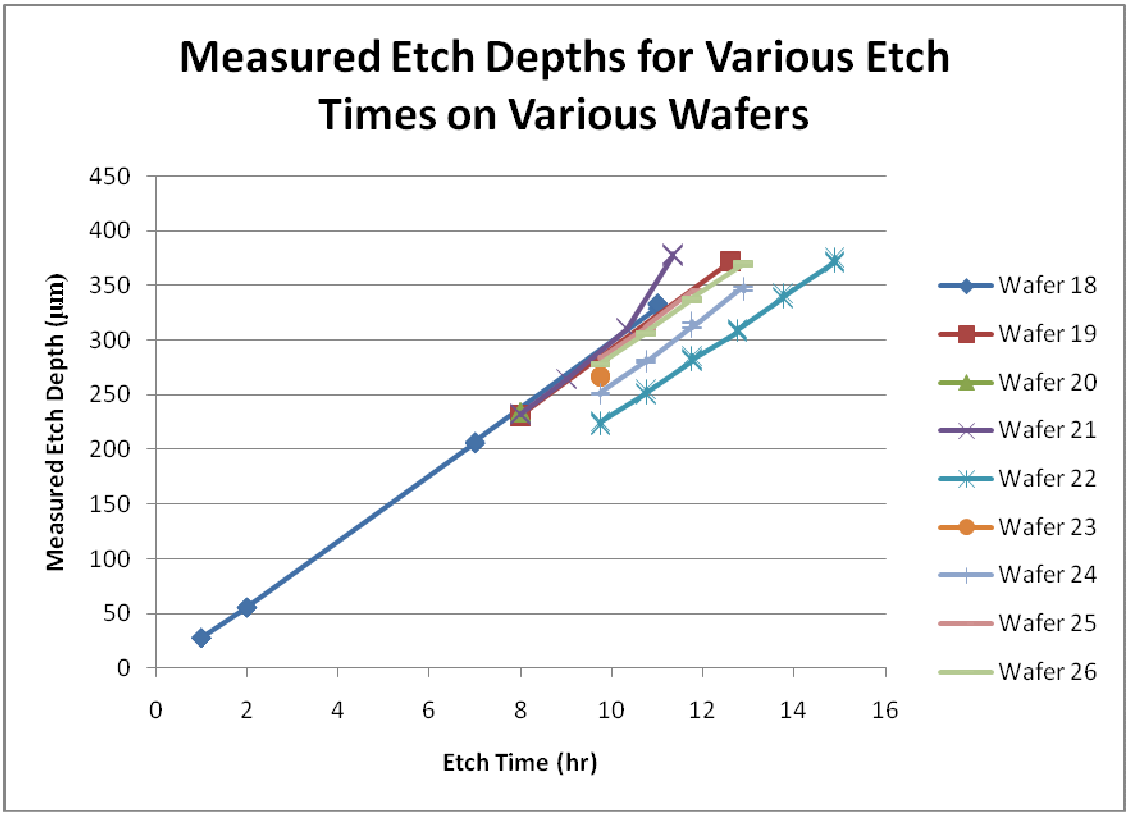

Figure 19: Etch depth as a function of etch time for various wafers showing the large differences in etch rates for the same parameters on similar wafers.

Table III: Table showing the etch rate of silicon in 25% by weight aqueous TMAH and R^2 value for various wafers.

Wafer	Etch Rate (μm/hr)	R^2 Value
18	29.936	0.9991
19	29.322	0.9981
21	30.857	0.8969
22	24.253	0.9718
24	26.443	0.978
25	29.151	0.9964
26	28.582	0.9984

3.6 Oxide Etch

The deep etching is now completed and the oxide mask is no longer needed. The oxide is etched away in BOE for the same amount of time as before for the masking process: 5 minutes 30 seconds. The oxide could remain there if a thermal and electrical boundary is desired but for this project it was not needed. Research has also shown that NiTi sputtered onto silicon has a shape recovery strain higher than NiTi sputtered onto SiO_2.[25]

3.7 NiTi Sputtering

The Cal Poly Select Series Rohwedder DC Magnetron Sputtering Machine was used to deposit the NiTi onto the silicon substrate. Previous works have characterized the sputtering process and this work confirmed their findings. The standard operating procedure was followed to pump down and prepare for the sputtering process. The Rohwedder has two separate targets, one of which can be covered to sputter with only one target. The wafer also has a cover in order to conduct pre-sputtering and clean both the chamber and targets. Both guns are separated by power and different power levels can be applied to each gun individually. For the NiTi sputtering one target was a 48/52 weight percent Ni/Ti and the other was 99.995% pure titanium. All Rohwedder targets were made by ACI Alloys Inc. and have a 2 inch diameter and 0.25 inch thick. The NiTi target was created from a Ni melt (99.99% pure) and a Ti (99.995% pure) melt melted together. To obtain a near 50/50 atomic percent mix of nickel and titanium the 346 W of power is applied to the NiTi target and 104 W of power to the titanium target. The chamber is first pumped to about 1.0×10^{-6} torr measured with both a hot cathode and

cold cathode pressure sensors. The cover for the wafer is made sure to be closed; this is to ensure there is no direct path of the targets' atoms to hit the substrate's surface during the pre-sputter process. Ultra high purity (99.999%) argon gas is pumped into the chamber leading to a pressure of about 2.2 x 10^{-3} torr. The guns are activated with their respective applied powers for 10 minutes while all the parameters are monitored as well as the plasma created in the chamber. After 10 minutes the guns are shut off and the argon valve closed. The system is left to reach equilibrium which takes about 10 minutes. New pressure readings are taken from both the hot cathode and cold cathode sensors; the pressure should be lower due to the titanium atoms gettering some of the oxygen and water vapor still in the chamber before the pre-sputter process. The argon is turned back on to a pressure of 2.2 x 10^{-3} torr and the guns reactivated. Once stabilized, the shutter for the wafer is opened and the material begins to deposit on the substrate wafer. This process goes on for about one hour which yields an approximate NiTi thickness of about 5 μm. The sputter rate was confirmed to be about 5.18 μm/hr. Once the deposition process is complete the shutter is closed, the guns shut off and the argon valve closed. The chamber is vented in order to change the target and measure the film thickness using the profilometer.

3.8 Chromium Sputtering

A thin film of chromium is sputtered on top of the NiTi to act as a diffusion barrier for oxygen during the annealing process. The current annealing process does not use a secondary pumping system like a diffusion or ultra-molecular pump to obtain lower pressures past 1 torr; therefore, a way to stop the diffusion of oxygen into the NiTi is needed. Oxygen that diffuses into the NiTi will react with the titanium and form titanium

oxide. Oxygen diffusion in chromium is low and therefore makes a great barrier. It also is easy to sputter and etch away without attacking the NiTi or silicon substrate. The same process for sputtering NiTi is used for chromium with only the NiTi target changed to a 99.95% pure chromium target. The titanium target remains since it is still activated during the pre-sputtering process to again act as an oxygen getterer. The applied is also changed to 425 W to the chromium target and only 90 W to the titanium target for pre-sputtering and 425 W for chromium target during sputtering. The titanium target is shielded and shut off during the sputtering process to prevent titanium sputtering and contamination respectively. The sputtering process only lasts for 10 minutes which yields a chromium thickness of about 500 nm with a sputter rate of about 86.9 nm/min.

3.9 Vacuum Annealing

The NiTi is now deposited onto the silicon substrate with a diffusion barrier on top; the NiTi must now be annealed and heat treated to crystallize and precipitate to obtain the correct transition temperature. Vacuum annealing is done due to the ease of titanium oxide formation in oxygen environments. A vacuum chamber was assembled with a heating chuck powered by the Rohwedder (Figure 20).

Figure 20: Picture of the vacuum annealing chamber used to crystallize and heat treat NiTi film.

A standard procedure was developed in order to be able to replicate the annealing done in the vacuum chamber and each wafer was annealed the same way. The wafer is placed on the heating chuck and the top replaced. The vacuum pump is turned on and left to pump down for about 30 minutes. This is to clean the chamber as best as possible prior to the annealing step. The vacuum pressure was found to be around 210 torr after the 30 minute pumpdown. After the allotted time, the heating chuck is activated from the Rohwedder system. The heating chuck begins to heat the wafer to 550°C, which takes about 5 minutes. After this heat up time, the 1-hour annealing time begins. Once the hour is over, the heating system is shut off with the vacuum system still running. The chamber will begin to cool to room temperature and the chamber cannot be vented until that time.

This is due to the introduction of oxygen into the chamber that could possibly diffuse at the elevated temperature. Another reason for waiting until the chamber is room temperature is to reduce the amount of chromium oxide formed (Cr_2O_3). This chromium oxide is more difficult to etch since the etch rate is much slower on the oxide over the pure metal. For easy of fabrication and processing, a lower amount of chromium oxide is desired.

3.10 RIE Etching

The NiTi thin-film is now crystallized and heat treated to shape memory and now the remaining silicon membrane must be etched away. Silicon with its high modulus will restrict the motion of the diaphragm, thus making it appear to not work as well as theoretical models say it should. Research has been done on silicon-NiTi diaphragms with much success.[29] The silicon could be etched away two different ways: dry etching or wet etching. Dry etching was chosen due to similar etch rates to wet etching but dry etching has better selectivity (Figure 21). Dry etching using a AG Plasma System 1700-Reactive Ion Etcher (RIE) was done on the backside of the wafer with no mask. The electric potential ionizes the argon gas and excites the oxygen gas.[30]

$$e^- + Ar \rightarrow Ar^+ + 2e^-$$

$$e^- + O_2 \rightarrow O_2^* + e^-$$

These then react with the source gas which is sulfur hexafluoride (SF_6).[30]

$$e^- + SF_6 \rightarrow e^- + SF_5^* + F^*$$

These reactive species then diffuse to the surface and adsorb onto the surface.[31] A surface reaction occurs creating silicon tetrafluoride which is a highly volatile compound that

desorbs from the surface and diffuses into the gas.[30] The volatile compounds are then pumped away by the vacuum pump attached to the chamber.[31]

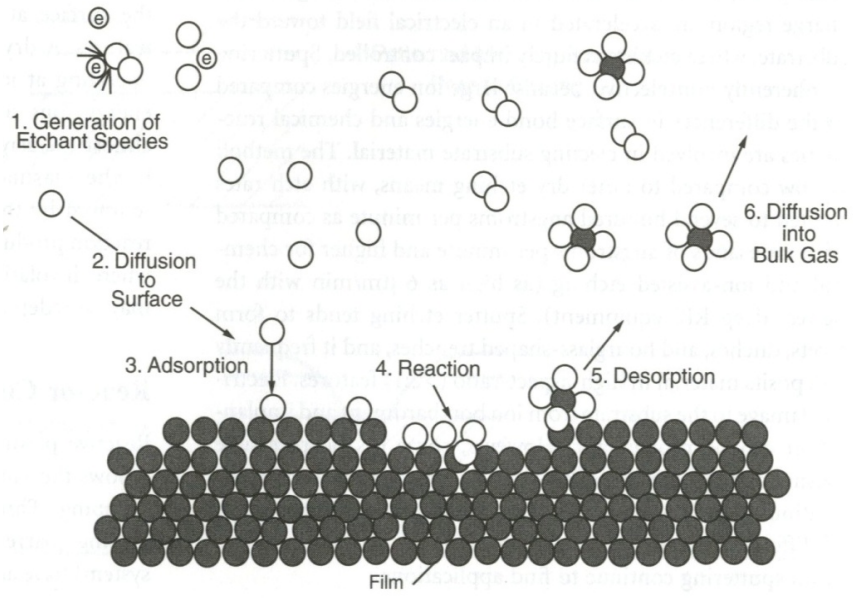

Figure 21: Diagram showing the various steps in a reactive ion etching process.[31]

Since there is only a thin silicon membrane remaining there would have been a small amount of etching to the thick section of the wafer and not affected the overall performance and properties of the wafer. Also, masking a wafer with a pit almost all the way through the wafer would have been difficult. It was found that using an 80:20 mix of SF_6 gas to O_2 gas had an etch rate of about 1 μm/hour and negligible etch rates to NiTi, chromium, and chromium oxide. This high selectivity made dry etching a perfect technique to etch the remaining silicon without affecting the other films.

The RIE was used following the SOP. The wafer was placed inside the chamber held in place with glass slides. The system was pumped down for about 30 minutes to ensure minimal contamination of air. A base pressure was recorded, which was typically

around 20 mtorr. Industrial grade (99.99% pure) SF_6 gas was flown into the chamber adding about 80 mtorr to the base pressure for a total of 100 mtorr. Once stabilized, ultra high purity O_2 gas was flown into the chamber adding about 20 mtorr to the base plus SF_6 pressure giving a total pressure of 120 mtorr. The 80:20 ratio has been set and the chamber pressure was set to 300 mtorr. The machine then moves a valve to obtain the selected chamber pressure while ensuring the same gas ratio. The RF power is then activated and the power set to about 300 W. Etch begins as soon as the power is turned on as there is no shield like that found in the Rohwedder. During the etching process, the DC bias between the cathode and anode was recorded as well as monitoring the plasma. The DC bias was initially found to be around 20 V and would lower as time went on usually ending around 6 V. The bias was unable to be controlled due to the current equipment only has a single power supply to create the plasma and the DC bias is created due to the gas mixture. Once the process was completed, the RF power was shut off as well as the SF_6 and O_2 gases. The chamber was then vented with low purity N_2 gas multiple times and finally the pump shut off. SF_6 gas is not lethal until high amounts, but to ensure maximum safety all the SF_6 gas was desired to be pumped out of the chamber prior to venting. Once the system was fully vented, the chamber was opened and the wafer was taken out.

3.11 Chromium Etch

Chromium etching was the last step in the diaphragm fabrication. The chromium was etched away in Chromium Etch 1020AC from Transcene. The etchant was heated in a glass beaker to about 40°C and the wafer dipped in the etchant. Agitation is recommended due to the slow etch rate of the oxide that is on the surface. The surface

will become hazy and will remain so until all the chromium is gone (Figure 22). Once the wafer is clear of this haze the wafer should be cleaned and dried.

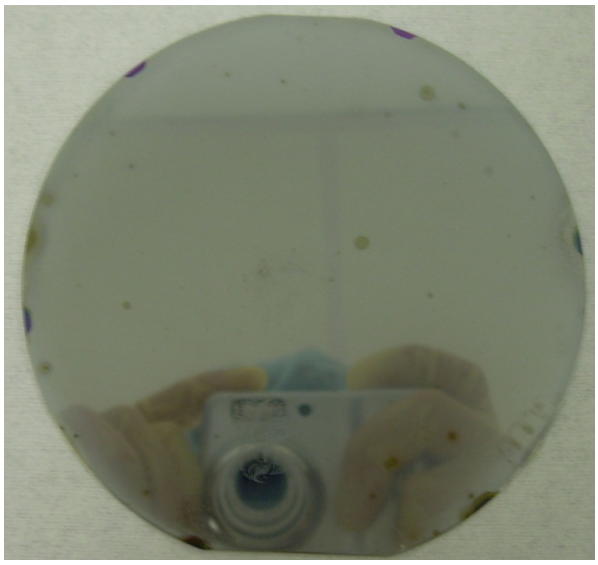

Figure 22: Picture of a wafer after five minutes of chromium etching. The spots show some of the hazy chromium and chromium oxide that shows further etching is necessary.

3.12 Cutting the Wafer into Individual Devices

The wafer mask contains small regions where the deep silicon etchant created small scribing lines around each device. These were used to break the wafer and cut the wafer into individual pieces for testing. The wafer was simply placed on top of a thin ruler and the scribe marks aligned to the edge of the ruler. The wafer was then snapped along the scribe lines as it is the largest defect in the silicon wafer.

3.13 Package Substrate Material & Preparation

Aluminum sheets were used to seal the diaphragm chamber; it was chosen due to the machineability and cost. Since holes are necessary in order to be able to apply pressure to the chamber through a tube the material has to be machineable. Also, the material must also be thermally conductive since it must transfer heat from a heating pad to the device. Aluminum has a high machineability thus making drilling and cutting much easier. The sheets were also inexpensive. The other materials considered were polycarbonate and glass. Polycarbonate is highly machineable and transparent allowing for the holes and diaphragms to be aligned easily. The problem with polycarbonate is the low thermal conductivity which did not allow for heat to pass through to the device easily. Glass is a great alternative to polycarbonate with the same transparency, but is slightly more difficult to machine and drill and is much more costly.

The process to prepare the aluminum was simple. Aluminum was bought in sheets with a thickness of 0.92 mm and cut into smaller pieces to fit one device per piece. Once the pieces were cut out, they were drilled in order to fit a small tube into the hole that could access the chamber.

3.14 Package Assembly

Multiple steps of bonding were necessary to fully contain and seal the device (Figure 23). Any leaks would lead to device failure and bad results. Various techniques were looked at in order to best bond and seal the chamber.

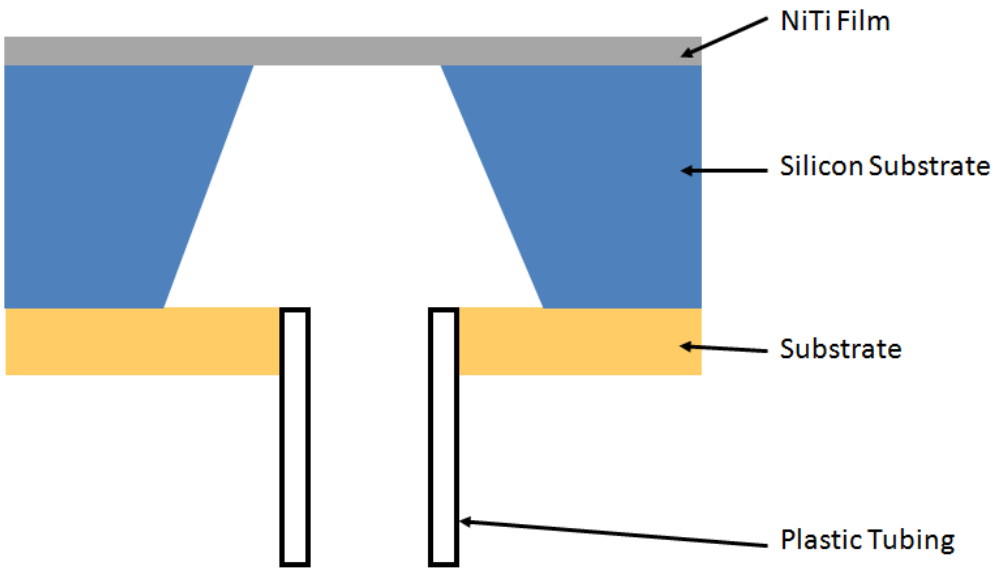

Figure 23: Diagram showing how the device would be packaged.

3.14.1 Types of Potential Bonding

Multiple methods of bonding the silicon substrate with the NiTi diaphragm to a package substrate that would seal the chamber, but allow pressure to be applied to the sealed cavity. Anodic bonding looked to be the most promising giving the strongest bond strengths and with no extra material needed like with adhesives. This proved difficult with current technology at Cal Poly so adhesives were looked at. Simple glues and epoxies dried too quickly to be used and UV curing epoxies were attempted. The cure times of the UV curing epoxies proved to be too long and difficult to achieve with the current technology at Cal Poly. The last method tried was using a silicone elastomer (PDMS) commonly used in our cleanroom for microfluidic chips as an adhesive. This proved to not only yield high bond strength, but was simple and easily reproducible.

3.14.1.1 Anodic Bonding

Anodic bonding was the first and ideal choice for this project since a lot of research has been done on anodic bonding in not only micropumps but other MEMS devices.[7] Anodic bonding also yields a hermetic seal and excellent bond strength far exceeding other bonding methods like the use of adhesives.[7] It can also be used to bond a large variety of materials like glass to glass, glass to silicon, glass to silicon compounds, glass to metals, and silicon to silicon with an inexpensive and simple set-up (Figure 24).[32] Heat is required to ensure diffusion of charged species occurs more rapidly and an electric field is necessary to move the charged species in the glass.[32] Applying the negative to the glass attracts the positive sodium ions leaving a relatively negative surface at the glass-silicon interface.[32] This negative region has many O2- ions which react with the silicon surface creating an oxide bond between the two materials.[32] Pyrex 7740 is the most common glass used for bonding due to the high amounts of sodium.[32]

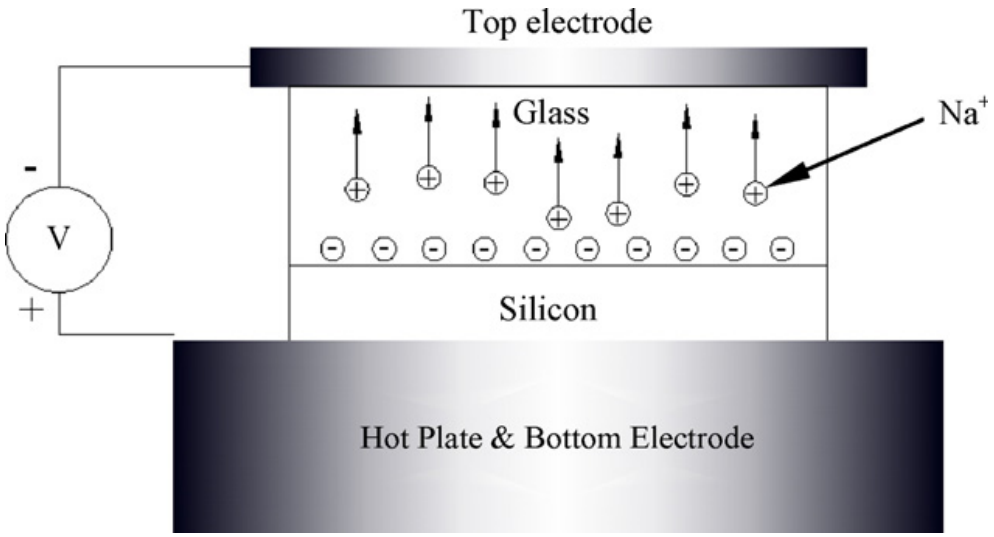

Figure 24: Diagram of a typical anodic bonding set-up showing the motion of the charges in the glass.[33]

Glass was able to be drilled leaving a great surface to bond silicon with, but the yield was found to be low usually around 50%. Anodic bonding proved to be difficult due to the use of N-type wafers with bonding times ranging from 45 minutes to 2.5 hours. At an elevated temperature of around 500°C for this amount of time would not only ruin the heat treatment of the NiTi but allow oxygen to diffuse into the NiTi and form a titanium oxide skin. All this oxide creation would rob titanium from the NiTi yielding a Ni-rich NiTi which would most likely give pseudoelastic properties. Glass could still be used to bond to silicon, but lower temperature process would be needed. Current anodic bonding techniques at Cal Poly are limited to high temperature low voltage bonding.

The reason the bonding took this long was due to the wafer selection. N-type wafers doped with phosphorous are electron rich leads to a difficulty in creating mobile positive charges.[34] The electron deficient p-type wafers doped with boron have a much easier time moving positive charges to the Si-glass interface and thus much more rapid bonding occurs.[34] If p-type wafers were to be used, anodic bonding could easily be used without ruining the heat treatment of the NiTi as research has shown complete anodic bonds in 4 minute at 300°C with only a 200 V bias.[34]

3.14.1.2 Epoxy & UV Curing Adhesives

An alternative would be simple adhesives like epoxy. These created a strong seal and bond between the glass and silicon, but due to the fast cure times, epoxy was unable to carefully spread around the silicon wafer prior to the hardening of some of the epoxy. An ultraviolet (UV) cure epoxy was then used in an attempt to bond the silicon device to glass. Norland Optical Adhesive (NOA) 61 and 81 were used which are low shrinkage

and fast curing adhesives respectively. Both yielded good results when it did bond, but it was found the cure times were too high and ranged from 3 hours to 12 hours. One of five samples of the NOA 61 adhesive bonded while three of five of the NOA 81 bonded after twelve hours. A UVP Blak-Ray B-100SP High Intensity Inspection UV Lamp was used to cure the UV curing adhesives. The recommended energy dose is 2 J/cm^2 at a wavelength of 365 nm. The UV lamp used puts out about 160 W at a wavelength of 365 nm. Due to the heat generation of the lamp, it was only left on for one hour at a time followed by a 30 minute cool-off period. This cycle was repeated in order to cure the adhesive. The lamp should have been able to cure the adhesive in a manner of minutes, but this was not the case. This was first believed to be due to the possibility that the light was being absorbed or reflected by the glass. But upon further analysis it was found that the glass used (Pyrex 7740) has a transmission of UV light at 365 nm above 80%. It was then realized that the lamp was too divergent and the majority of the light was being lost and not hitting the small device package.

3.14.1.3 Polydimethylsiloxane

Polydimethylsiloxane, or PDMS, was the silicone rubber that was then used with great results. It was easy to mix, syringe onto the silicon and had a low heat treating temperature. The cure time at room temperature is much longer than the time it took to syringe the PDMS onto the silicon wafer (which took about 15 minutes). At this point, polycarbonate was being used as a substrate material due to the lower cost and superior machinability than glass. The PDMS used was Sylgard 184 silicone elastomer two-part kit with a base and curing agent. The recommended ratio was a 10:1 base to curing agent by volume. The base and curing agent were mixed together and degassed. They were then

placed into a syringe and dispensed along the wafer. The package was then placed in an oven at 80°C for about one hour. This yielded a strong and mostly air-tight seal.

3.14.2 First Level Bonding – Silicon Substrate to Package Substrate

Polydimethylsiloxane was found to be the best way to bond the silicon wafer and aluminum (Figure 25). About 10 mL of base was measured in a syringe and put into a cup with about 1 mL of curing agent. The two were mixed in the cup and placed into a vacuum chamber. The vacuum chamber was then turned on and all of the air from mixing was pulled out of the PDMS mixture. This mixture was then placed in another syringe and syringed onto the silicon wafer devices careful not to place any near the pit. PDMS on the NiTi membrane would negatively affect the performance of the device due to the added material. The aluminum piece was then brought in contact with the PDMS on the silicon wafer ensuring the hole was properly aligned with the membrane on the opposite side of the silicon wafer. This package was then placed in an oven at 80°C for one hour, as recommended by the PDMS manufacturer. The package was then taken out of the oven after one hour and allowed to cool. The bond was examined to ensure the PDMS was fully cured; if not, the device was placed back in the oven for more time.

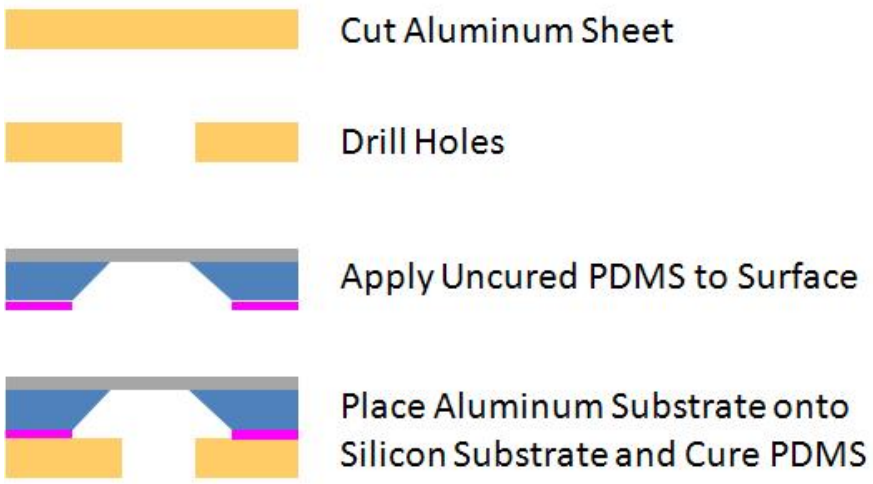

Figure 25: Diagram of how the aluminum substrate was prepared, PDMS was applied to the silicon surface and the bonding between the aluminum substrate and silicon wafer.

3.14.3 Second Level Bonding – Sealing the Package

The package now needed to be sealed on the sides to ensure there are no leaks through the PDMS. The excess PDMS mixture was then syringed on the boundary between the silicon wafer and aluminum substrates (Figure 26). The package was then placed in the oven again for another hour. After this time the seal was examined in order to see if the PDMS was fully cured or not. If not, the package was placed in the oven for more time.

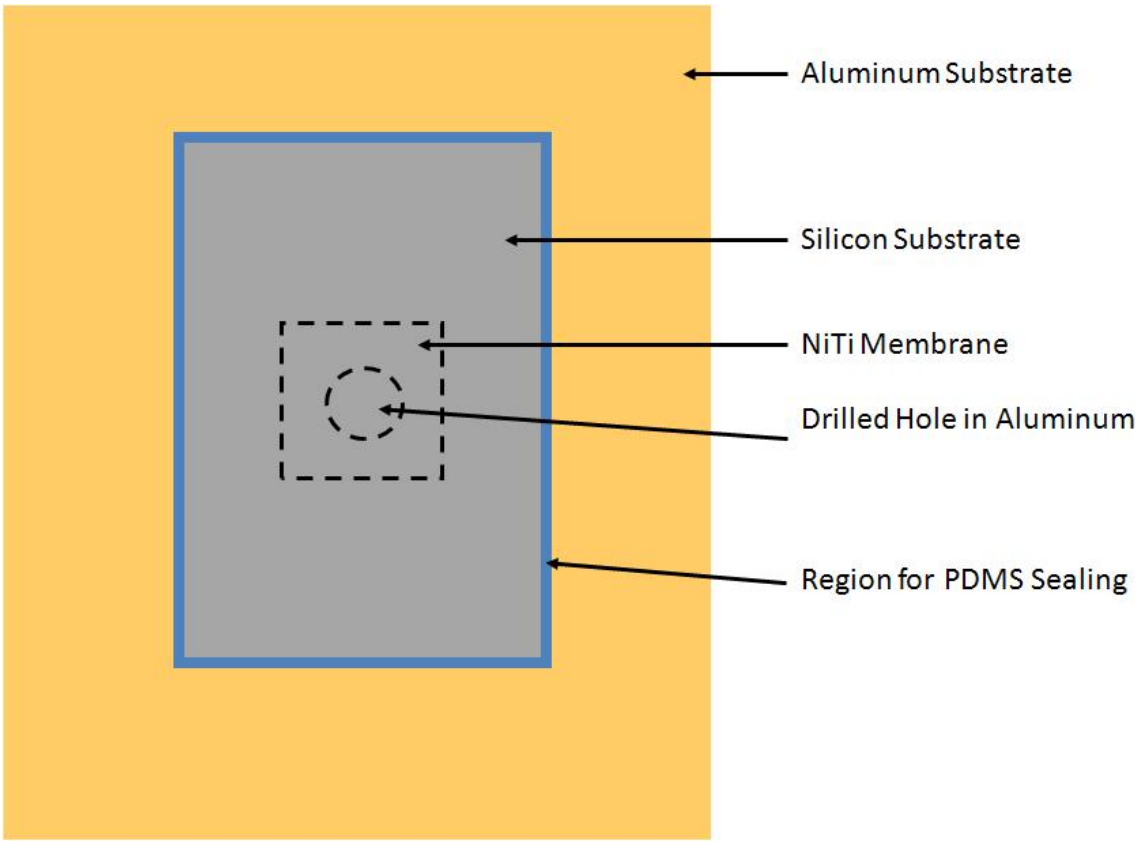

Figure 26: Diagram showing how the device package was sealed after the first step of bonding to the aluminum substrate.

3.14.4 Third Level Bonding – Sealing the Tubing

The last step in the package fabrication was to insert the plastic tubing into the drilled hole and seal in place (Figure 27). The tubing was inserted into the drilled hole careful not to touch or damage the diaphragm. The same PDMS mixture was then syringed around the tubing and the entire package placed in the oven for one hour. The package was then taken out and examined to ensure the PDMS was fully cured and the tubing held in place. If not, more time in the oven was needed. The final device package was now fully assembled and ready for testing (Figure 28).

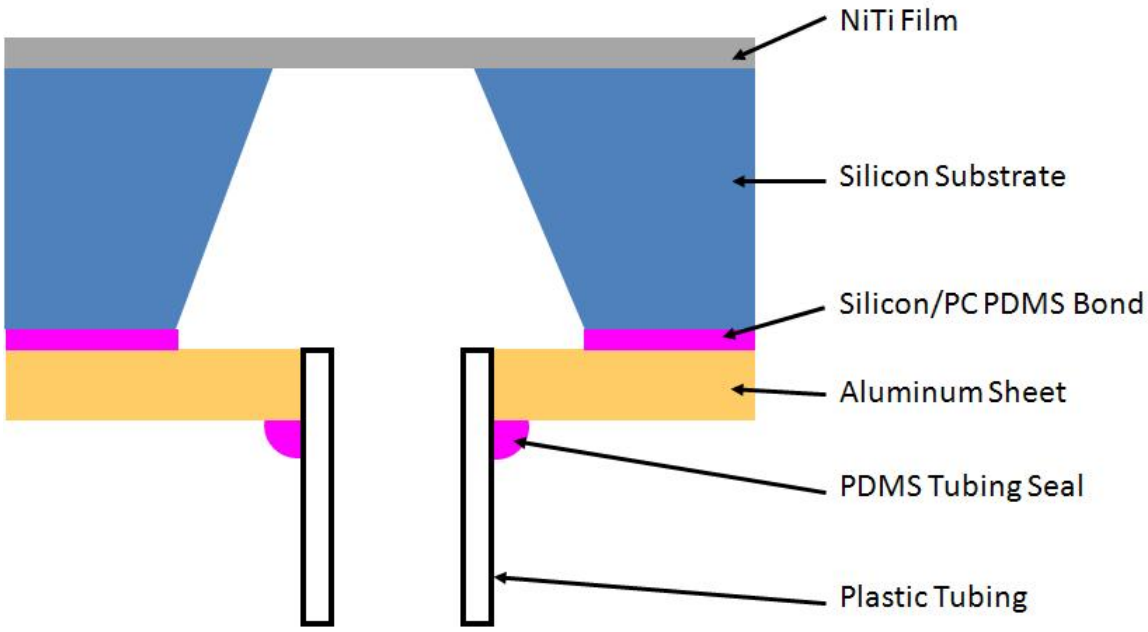

Figure 27: Diagram showing how the tubing was inserted and sealed to allow air to enter the chamber and applied a specified pressure.

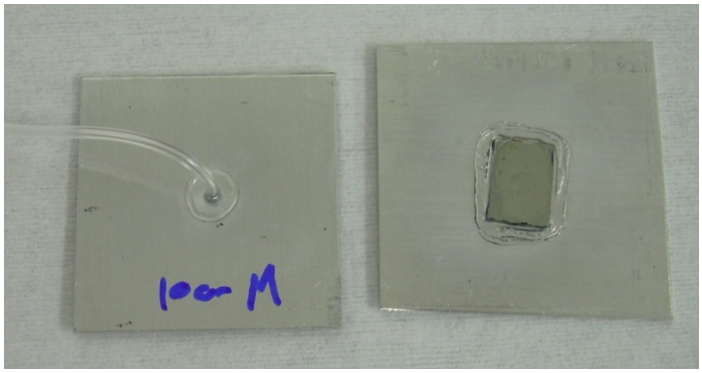

Figure 28: Picture of both sides of a completed package. The tubing can be seen coming out of one side (left) while the device is bonded and sealed on the other (right).

3.15 Testing System Design

A system had to be designed in order to be able to accurately measure the applied pressure to the NiTi membrane while measuring the maximum deflection. The system utilized a heating element to raise the temperature of the device above the A_f temperature of the annealed NiTi (Figure 29). This system was created using a nitrogen tank with various regulators to reduce the pressure from 14710 kPa (150 kg/cm^2, 2133 psi) to around 5 to 225 kPa (0.725 to 32.6 psi). There is a lead to a 4-way valve that is connected to both a pressure sensor and the tubing connected to the test device. The pressure sensor is able to read the pressure applied and since it would be in parallel with the device and both ends were sealed, a uniform pressure would be attained within moments of opening the nitrogen tank valve. There was minimal gas leaking and the nitrogen tank was able to counteract any gas loss so a uniform pressure was attained throughout the profilometer scanning process. The other line was connected to the Tygon tubing sealed into the device with a simple mechanical seal with a needle. The final test set-up without the heater is shown in Figure 30.

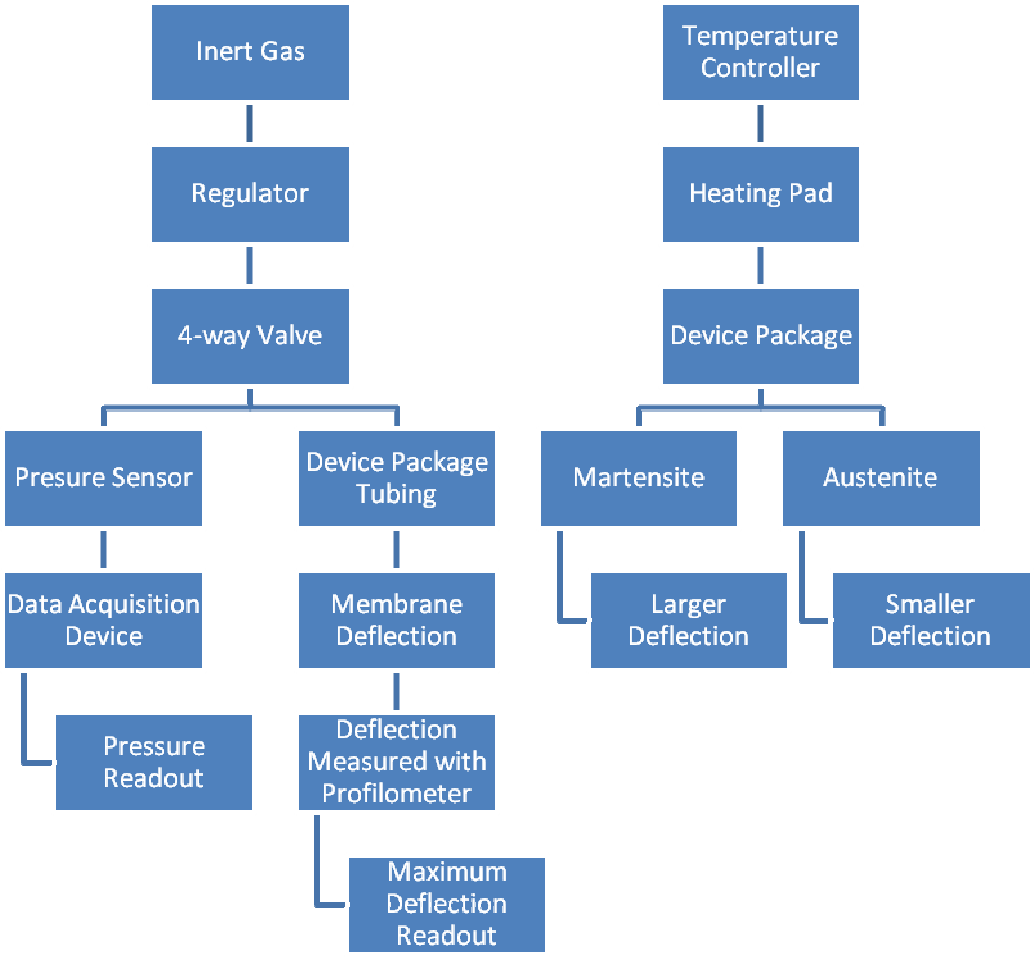

Figure 29: Diagram of the testing system flow chart showing the various parts necessary for testing.

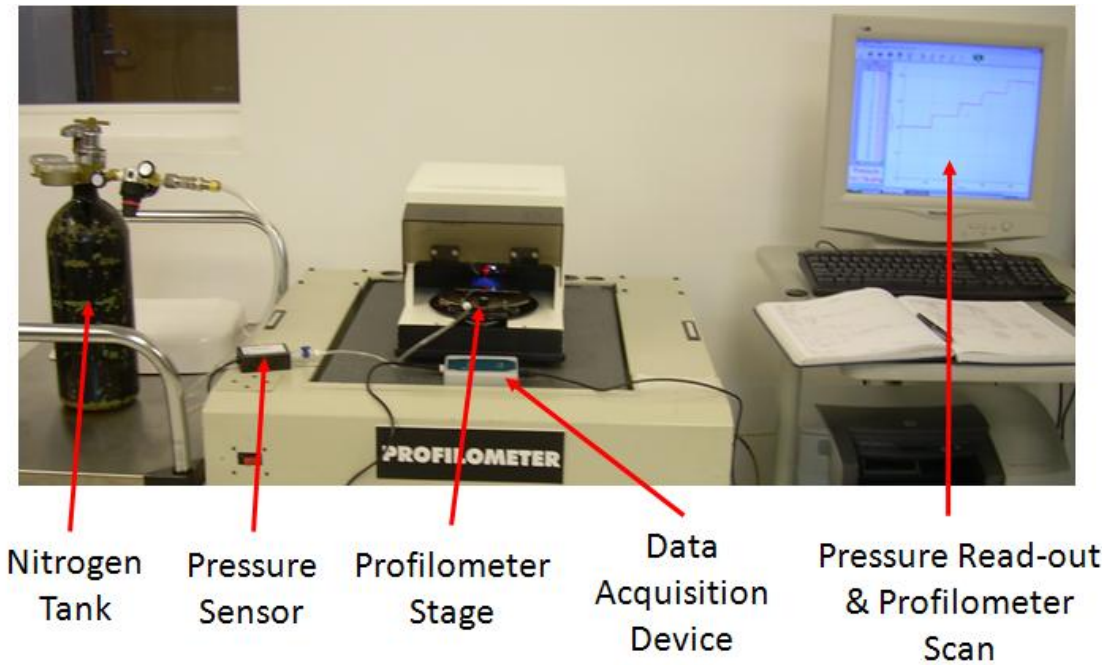

Figure 30: Picture showing the overall testing set-up and the key components.

A test stand also was needed to be constructed in order to allow the device to lie flat as well as allow the tubing on the backside to be connected to the system. This was done with a thick (0.5 in) aluminum block that had a notch milled into it (Figure 31). This allowed for tubing to be connected to the nitrogen line and pressure sensor as well as giving a flat surface for the device to sit on. The same set-up was used for the elevated temperature scans but with a temperature controller activating the heating pad below the aluminum block (Figure 32). A thermocouple between the aluminum block and heating pad allowed for a feedback loop back to the temperature controller which led to a small temperature deviation from the set-point. The temperature controller was allowed 10 to 15 minutes to heat the stage to the set temperature, which was enough time for the system to come to equilibrium and uniform temperature prior to testing.

Figure 31: Picture showing the aluminum block with the notch allowing for the Tygon tubing to pass through while still giving a flat surface to test the deflection.

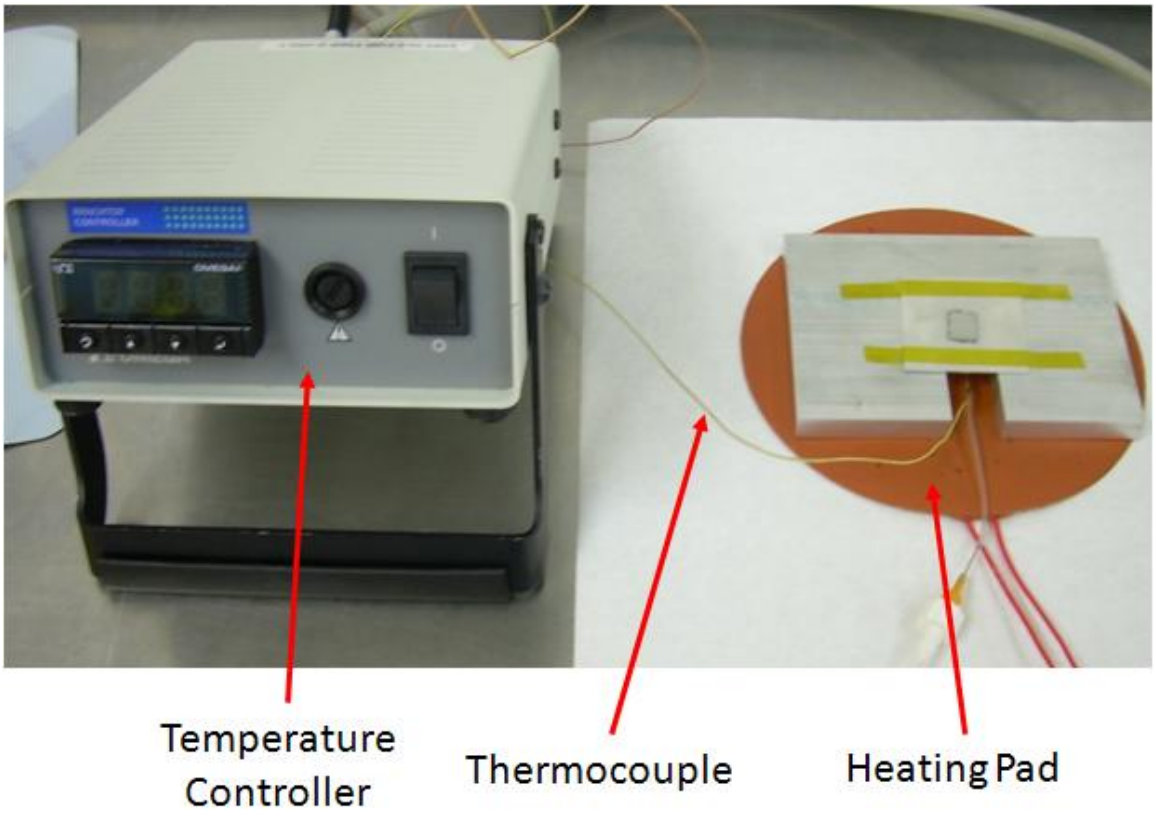

Figure 32: Picture showing the full test set-up outside of the profilometer complete with the temperature controller, thermocouple and heating pad.

The device was also tapped down onto the aluminum block to ensure no movement during the profilometer scans which could greatly affect the results of deflection (Figure 31). Kapton tape was used for this due to its ability to withstand higher temperatures without noticeable loss in strength or adhesion.

3.16 Testing

The deflection of the membrane was measured with the profilometer (Figure 33). This was due to the high sensitivity with the z-axis range of the deflection membrane. The devices were lined up as best as possible and moved around in order to find the absolute maximum deflection with each situation. Testing also conducted 90˚ from the diagram below to ensure no difference in the maximum deflection, so all the data presented was the maximum found in the orientation below.

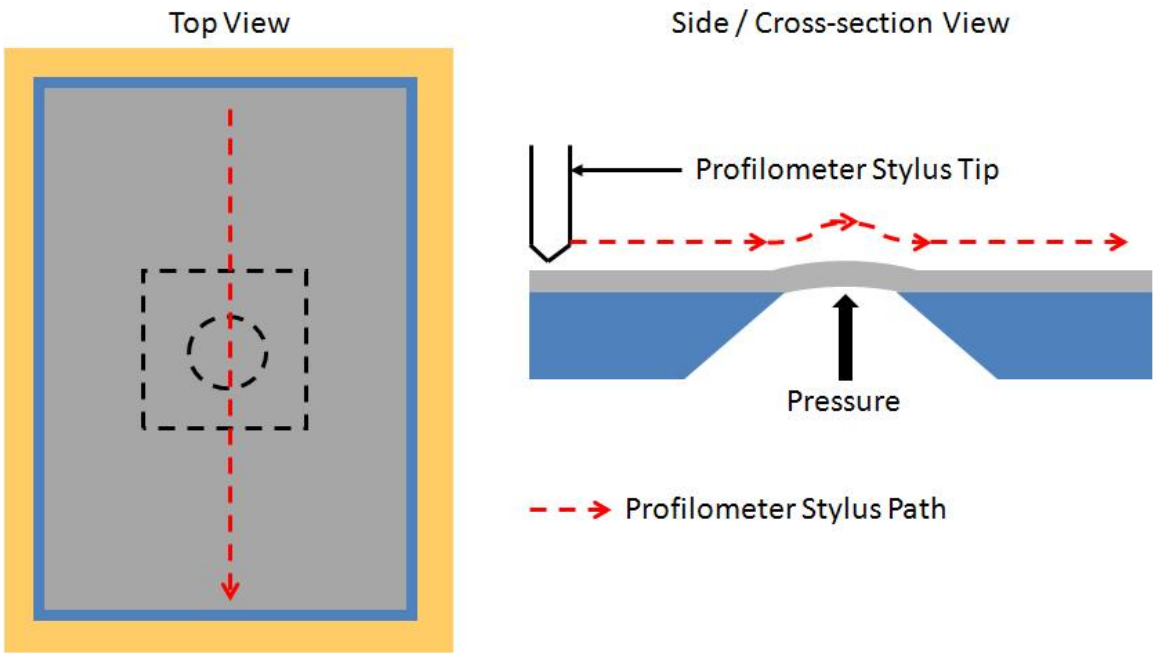

Figure 33: Diagram showing the profilometer stylus path used for testing the maximum deflection of the NiTi membranes.

3.17 Material Characterization

It was desired to be able to test the NiTi thin film and ensure similar results to previous work.[11,12,20] Differential scanning calorimetry (DSC), energy dispersive spectroscopy (EDS), and x-ray fluorescence (XRF) were the three main characterization techniques that were considered.

3.17.1 Energy Dispersive Spectroscopy

Due to the small compositional tolerance for NiTi to be shape memory, compositional analysis was conducted with both EDS and XRF. XRF would yield an easy to obtain answer but might not be as accurate as EDS. Using a Joel JSM-6390 SEM with an attached Thermo Scientific EDS system, an area was imaged and an area map of

the composition was conducted (Figure 34, Figure 35). The composition was then found using the software (Table IV). The composition was found to be slightly titanium rich by weight percent which means a slightly nickel rich by atomic percent. There was also negligible oxygen and chromium within the NiTi film. This shows the chromium diffusion into NiTi and oxygen diffusion through chromium are negligible. The low amounts of aluminum found in the NiTi film can be traced back to similar impurities found in the NiTi and Ti sputtering targets.

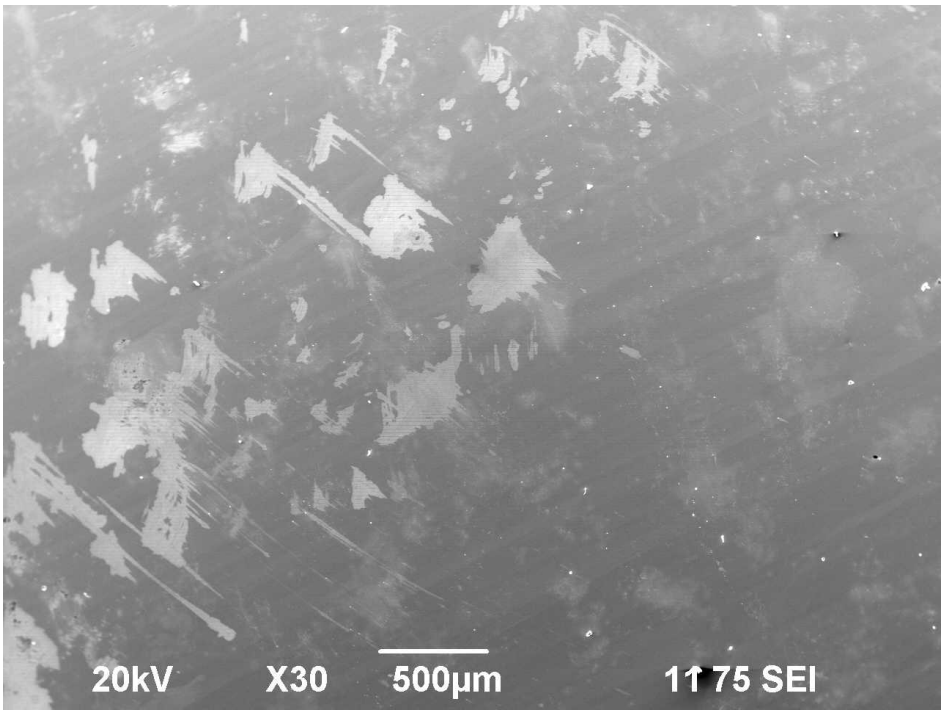

Figure 34: Micrography of the NiTi surface used for the EDS analysis.

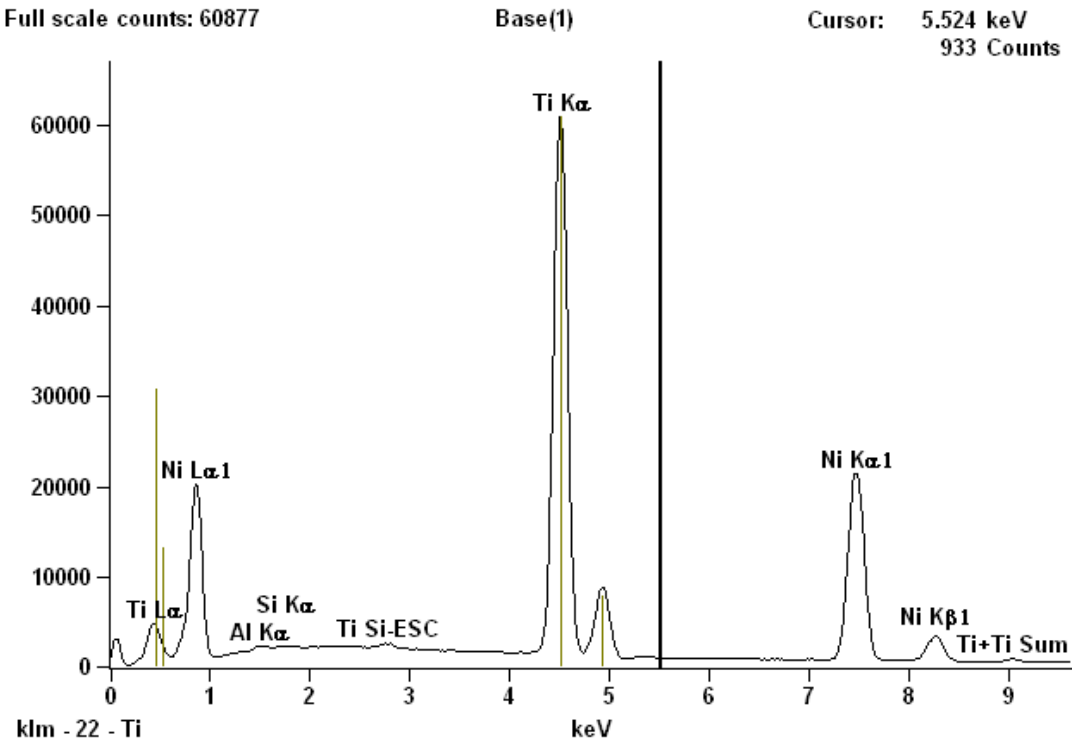

Figure 35: EDS spectra of an area map taken on a NiTi thin film, post annealed and Cr etched.

Table IV: EDS measured values of a sputtered NiTi thin film, post annealed and Cr etched. No detectable oxygen or chromium indicates negligible diffusion of oxygen and chromium into the NiTi.

Element	Weight Percent ± Standard Deviation
Nickel	47.09 ± 0.33%
Titanium	52.67 ± 0.20%
Aluminum	0.22 ± 0.03%
Silicon	0.04% ± 0.01%

Figure 34 shows two regions with different contrast, but it was found that the composition was the same in both regions (Table V). This difference in color might be due to different crystal phases, since full crystallization is unlikely due to the non-equilibrium conditions during the annealing step. Further analysis is out of the scope of

this project. Since the deflection measured was found to be similar to what was expected of martensite the majority of the microstructure should be martensite. Due to the abundance of dark regions found on the surface of the film, it is believed that the dark region is martensite while the less abundant white region is austenite.

Table V: White and dark region compositions compared showing little difference in composition.

Topography Region	Weight Percent ± Standard Deviation			
	Nickel	Titanium	Aluminum	Silicon
White Region	47.01 ± 0.33%	52.74 ± 0.20%	0.25 ± 0.03%	N/A
Dark Region	47.16 ± 0.33%	52.59 ± 0.20%	0.18 ± 0.03%	0.08 ± 0.03%

3.17.2 X-Ray Fluorescence

XRF was also used to find the composition of the NiTi thin film. The composition found was almost identical to what was found using EDS but with a larger standard deviation (Table VI). This can be used to easily and quickly find the composition of the NiTi film before further processing is conducted.

Table VI: XRF measured values of percent of Ni and Ti in a sputtered film post heat treatment and chromium etching steps.

Element	Atomic Percent	Weight Percent
Nickel	52.34%	47.25%
Titanium	47.66%	52.75%

3.17.3 Differential Scanning Calorimetry

To prepare samples for differential scanning calorimetry (DSC) the wafer process was adapted from the standard procedure from previous sections. The wafer was oxided but not masked and NiTi followed by chromium was sputtered. The wafer was then annealed in the vacuum annealing chamber and allowed to cool under vacuum. The wafer was then etched with the chromium etchant. The wafer was then scribed and broken in order to rip the NiTi off the oxide surface. Once the wafer was fractured, some of the NiTi delaminated allowing for removal from the oxide and silicon substrate. This was then cut into separate samples for analysis. DSC analysis was conducted following ASTM standard F2004-05. The DSC used for this analysis was a Q-1000 from TA Instruments. The sample size could only be around 1-5 mg due to the size of the pans, so that was different than what was recommended in the ASTM standard. The cooling and heating rate was 10 °C/minute. The standard recommends going 30 °C above the estimated austenite finish temperature and 30 °C below the estimated martensite finish temperature. Since the finish temperatures were not known at all, the high was set to 200 °C and the low was set to -50 °C. The procedure for the DSC scan included an eqlibriate step at 30 °C followed by a ramp to 200 °C at 10 °C/minute. The DSC then cooled the sample and reference pan to -50 °C at 10 °C/minute followed by a return to 30 °C at the same heating rate.

Chapter 4 - Experimental Results & Discussion

4.1 Process Yield

Due to the extensive amount of processing, the final device yield was quite low (Table VII). The steps listed were the only steps that caused a loss in devices while all the other steps did not have any noticeable device loss.

Table VII: Approximate process yields and total yields for the critical processing steps for fabrication of the NiTi diaphragm package.

Process Step	Process Yield (%)	Total Yield (%)
Oxide Masking	75	75
Deep Silicon Etching	30	23
Vacuum Annealing	90	20
Bonding to Substrate	50	10
Sealing the Package	75	8

The oxide masking loss was due to non-uniformity of the photoresist during the spin coating process. Most of the wafer would be coated correctly, but there would always be regions on the wafer where the photoresist did not adhere well and oxide was left exposed. Many steps were taken in an attempt to minimize device loss during the masking step, but nothing proved to work. Deep silicon etching was the step that had the most device loss and the lower yield. This was due to flaws in the oxide mask where the etchant would quickly attack certain regions and not others. Many holes and pits were found in the wafer in regions where they should not have been. Also, many holes were found in the etch pits even after only a few hours of etching. These flaws were difficult to predict and prevent, and thus a low yield occurred. The vacuum annealing step seemed to damage a few devices, which is most likely due to regions of high film stress. These

regions would attempt to relieve the stresses, but in doing so cause delamination or cracking on the surface. This was found only in a few devices and did not seem to be a major problem.

Bonding the device to the substrate and sealing the packing and tubing all seemed to have device loss as well. This was caused by the PDMS leaking into the chamber and curing inside. This caused the membrane to not deflect since the membrane was glued to the substrate and not free-floating over the chamber. These were also difficult to avoid and could only be prevented by minimizing the amount of PDMS to bond the device to the aluminum substrate.

4.2 NiTi Device Performance

The devices were tested and their maximum deflections were measured at various pressures (0, 10, 20, 30, 50, 75, 100, 125 kPa above atmosphere) and at two different temperatures (20 ˚C and 60 ˚C). Different sized devices were tested in order to see the effect of size on the amount of deflection. Also, the theoretical deflection was compared to the actual deflection of the devices (Equation 1). The deflection (z) of a square membrane is a function of applied pressure (P), membrane size (a), Poisson's ratio (ν), elastic modulus (E), and thickness (t).[27] A regression model was used to analyze the effects of pressure, membrane size, temperature and theoretical versus actual deflection. The final device package is seen below (Figure 36).

$$z = \frac{0.01518Pa^4(1-\upsilon)^2}{Et^3} \qquad \textit{Equation 1}$$

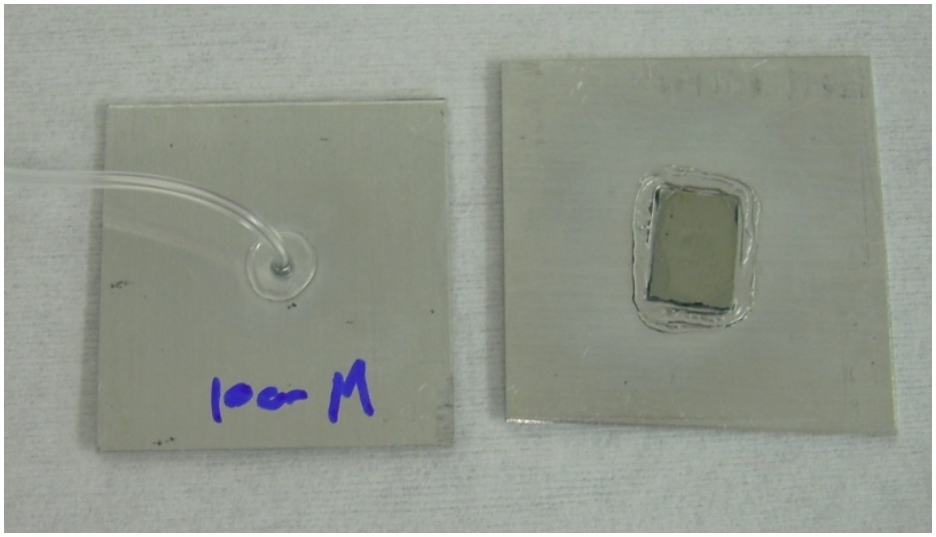

Figure 36: Picture of the device fully packaged and ready for testing. The left shows the backside with the tygon tube coming out and the right shows the front side with the NiTi membrane.

4.2.1 Effect of Pressure

The effect of pressure was found to be significant with a p-value less than 0.01 which matches the scatter plot below (Figure 37). The effect of pressure was also found to be linear, though there was not enough data to run a meaningful statistical analysis. This agrees with the theoretical model, which means the effect of pressure can easily be predicted.

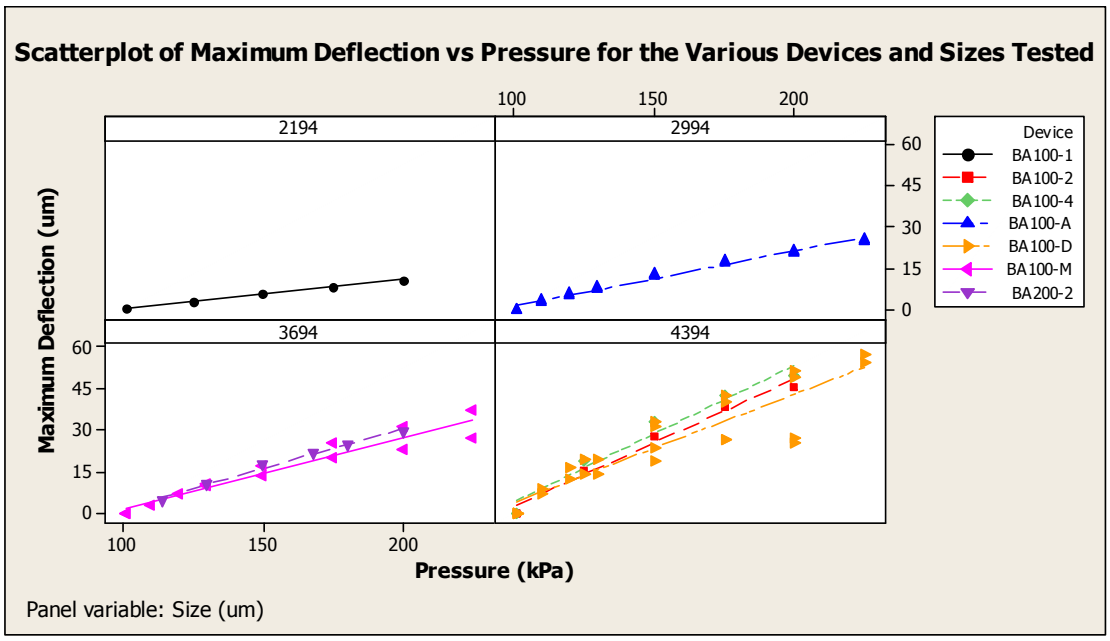

Figure 37: Scatterplot of the maximum deflection as a function of pressure for various sizes (2194, 2994, 3694, and 4394 µm) of membranes tested showing the highly linear relationship between pressure and deflection.

4.2.2 Effect of Membrane Size

The effect of membrane size was also significant with larger membranes yielding much higher deflections with a p-value less than 0.01 (Figure 38). Again, this agrees with the model but not enough data is available to show whether or not the trend is to the quartic. More samples and sizes are needed to ensure whether the effect of membrane size is quartic as the theoretical model indicates.

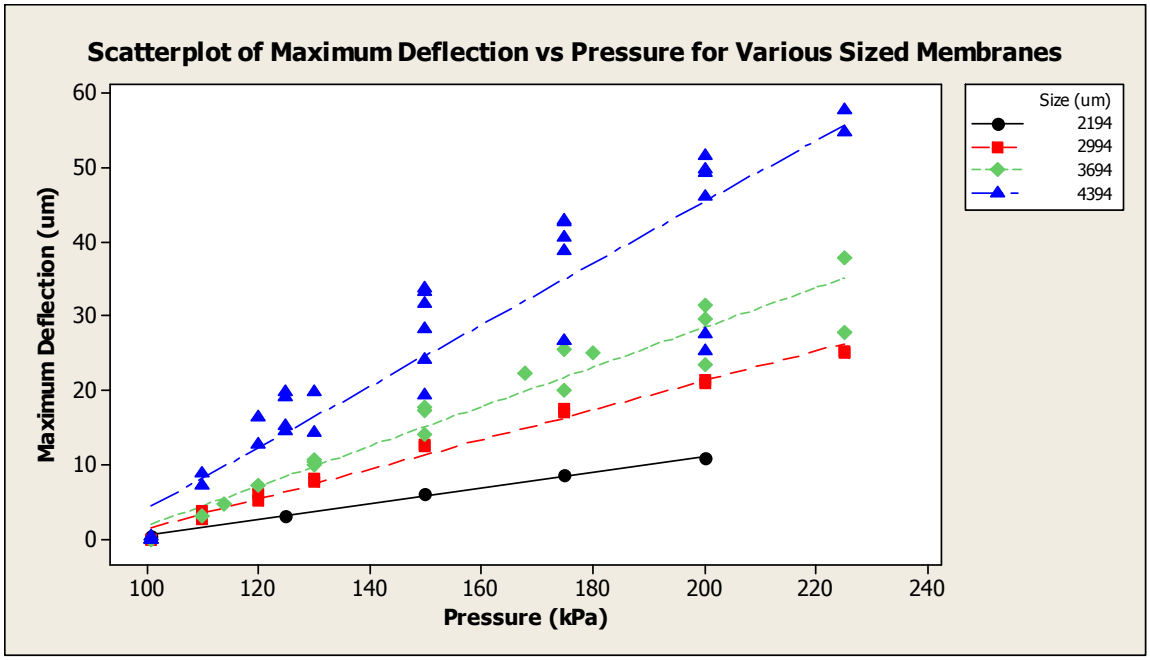

Figure 38: Scatterplot of the maximum deflection as a function of pressure showing the higher deflections obtained with larger membranes tested.

4.2.3 Theoretical vs. Actual Deflection

The theoretical deflection expected for the given parameters for each device were calculated and compared to the actual deflection measured. There was also a significant difference between the theoretical deflection and the actual deflection with a p-value of less than 0.01. It was found that five of the seven devices tested showed inferior performance when compared to theoretical while two showed superior performance.

4.2.3.1 Devices with Inferior Performance

Most of the devices showed inferior performance when compared to the theoretical models, especially at higher deflections. This was seen in the 3694 µm and 4394 µm membranes (Figure 39). The average difference was found to be around 30%.

The lower amount of deflection observed in these samples is most likely due to unetched silicon on the membrane surface during the RIE dry etching process. Some preliminary work showed that the uniformity etching in the RIE across a single wafer is low and can vary up to ±10-15%. The remaining silicon has a much higher elastic modulus than the NiTi membrane, which according to *Equation 1* would lead to a much lower deflection. To have an approximate decrease of 30% deflection only around 3.5 µm of silicon would need to remain. Given that around 10 µm of silicon was remaining prior to RIE etching, it is feasible that enough silicon would remain, diminishing the amount of deflection of the NiTi membrane.

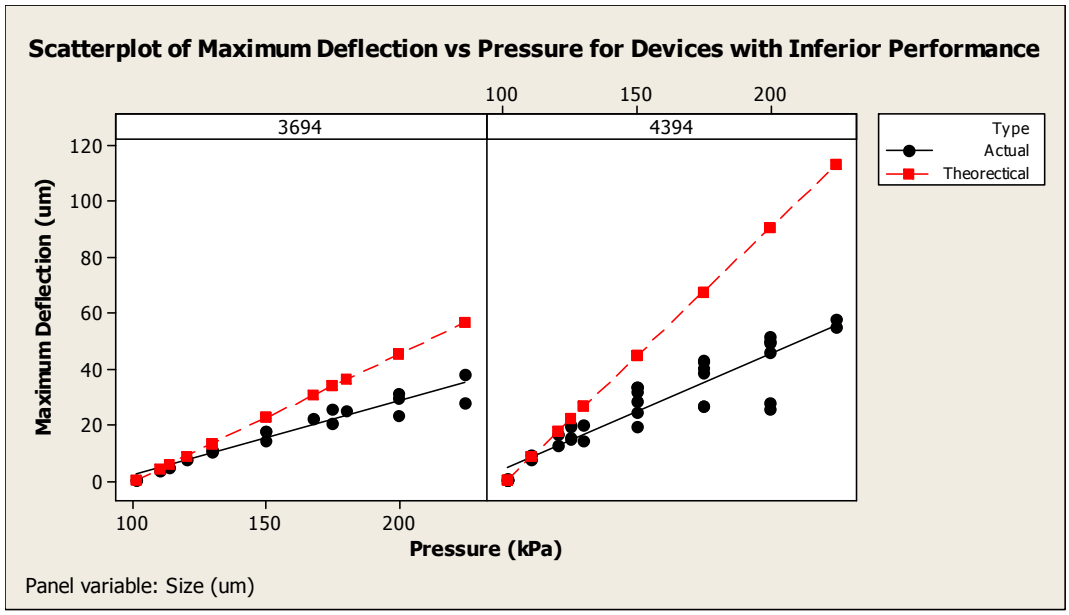

Figure 39: Scatterplot of maximum deflection as a function of pressure showing devices with inferior performance when compared to the theoretical model.

4.2.3.2 Devices with Superior Performance

A minority of the devices showed superior performance when compared to theoretical model. At first this does not make sense, as the model assumes a perfectly homogeneous and uniform film, which should yield the best performance.

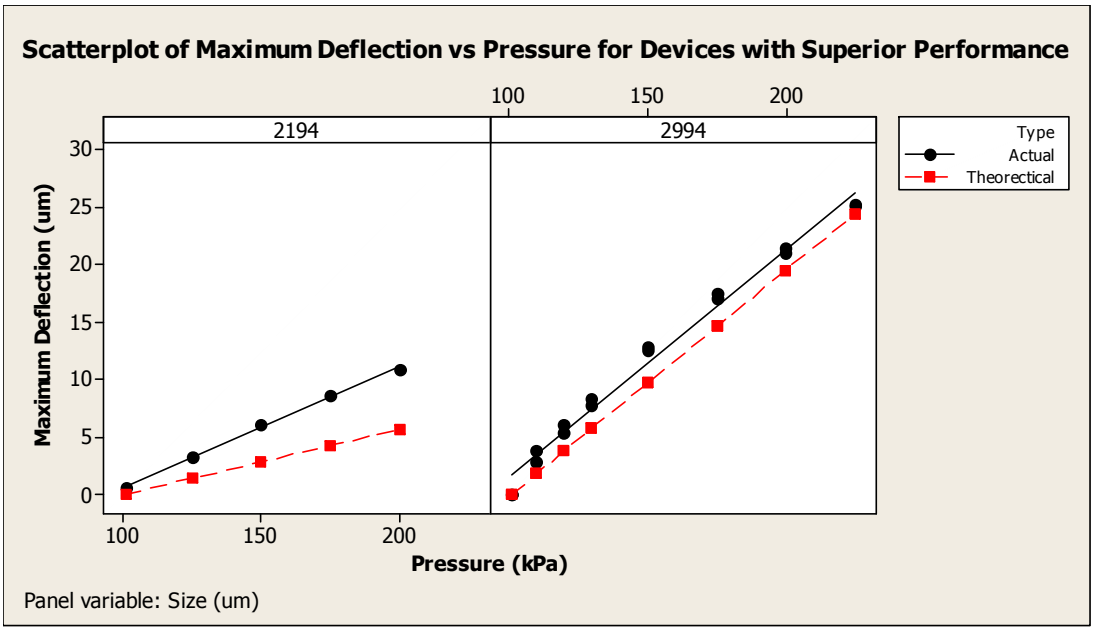

Figure 40: Scatterplot of maximum deflection as a function of pressure showing devices with superior performance when compared to the theoretical model.

There are a few possibilities when looking at the model to see where a superior performance could be achieved. At first the elastic modulus could be wrong. But EDS and XRF confirmed the composition and combined with the phase diagram, the majority of the material should be NiTi. The amount of precipitates to create a significant change in modulus would have to be much higher. Film thickness uniformity could be another problem; a thinner film would lead to more deflection. This also cannot be the case as the sputter rate across a wafer was confirmed to be within ±5% from the center to the edge. Also, as seen in *Equation **1***, deflection is function of thickness cubed as opposed to the

membrane size which has a quartic effect. The sputtering system rotates the substrate above the targets yielding a highly uniform film. Poisson's ratio is a material property and could not be easily changed, and pressure was measured and calibrated. The last possibility is the membrane size. At first this also seems unlikely since NiTi has a strong adhesion to silicon.[11,12,19] As mentioned before, size has a quartic effect on deflection and with an approximate 45% increase in deflection, only a 2.6% increase in membrane size would lead to the observed increase deflection. A 2.6% increase in membrane size could be achieved due to delamination at the NiTi and silicon interface or lateral etching of silicon. Both of these processes could be achieved during the RIE etching process and both could yield membranes which could be slightly larger than expected (Figure 41). This means that the 2194 μm membrane and the 2994 μm membrane would only need to increase by 57 μm and 78 μm respectively to obtain the observed deflection at the applied pressures.

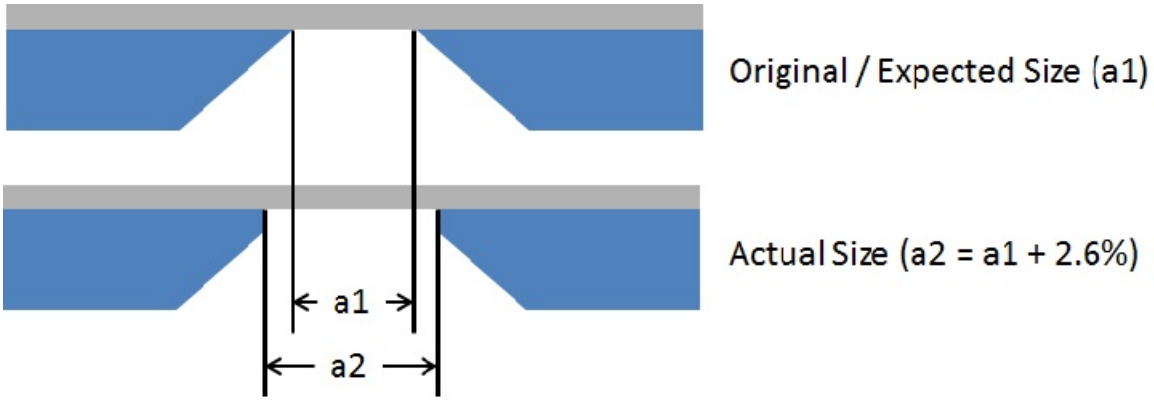

Figure 41: Size increase during RIE etching that could lead to a larger membrane yielding much higher deflections than expected.

Reactive ion etching of silicon is highly anisotropic, but it is not fully anisotropic. There is a slight etching of the side walls and research has shown that there can

sometimes be extensive etching of the sidewalls and low selectivity of the ratios used for this process (Figure 42).[35] With the 80:20 SF_6 to O_2 gas ratio, this leads to an approximate anisotropy of 0.9 and a selectivity of 12. This means that during the 10 μm silicon etch can lead to an increase in membrane size of 1 μm. This was not the case as the devices were approximately the expected size; this could be due to the fact that the RIE silicon etch is blanket etch with no mask to protect the silicon. The large amount of silicon volatile by-products could be saturating the gas causing a lower etch rate. This would also explain why some devices showed inferior performance since all the silicon was most likely not fully etched away.

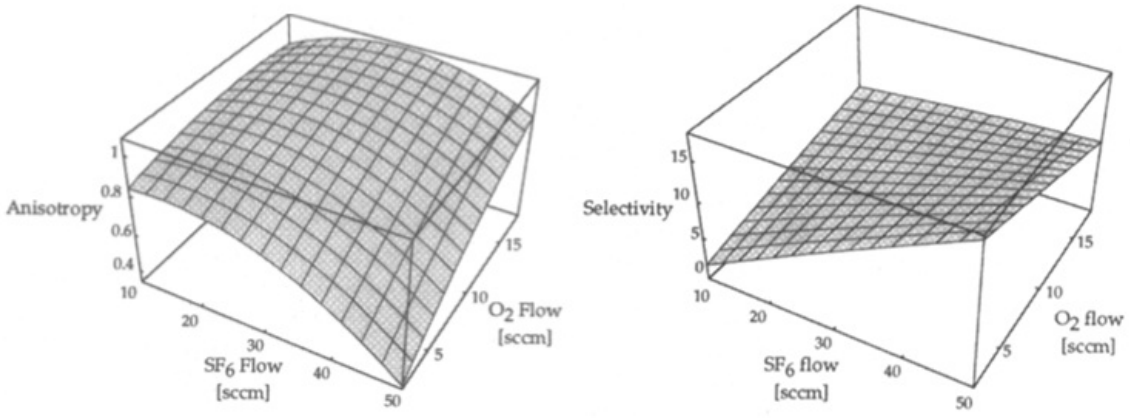

Figure 42: Diagram showing the anisotropy and selectivity of RIE etching of silicon.[35]

Delamination is also likely due to the high reactivity of titanium and oxygen. It is believed that due to the introduction of oxygen to the membrane that it will react with the titanium forming a titanium dioxide layer. This oxide layer can then delaminate from the silicon or NiTi which can also create a larger than expected membrane (Figure 43).

Figure 43: Diagram showing the mechanism of delamination during the RIE process that would yield a larger than expected membrane.

4.2.4 Effect of Temperature

Temperature was found to not have a significant effect on the maximum deflection of the devices tested with a p-value of 0.354. This was unexpected as the membrane should have experienced a phase change from martensite to austenite. Martensite with its elastic modulus of around 45 GPa should have experienced a much higher amount of deflection with same conditions as austenite which has a much higher modulus of around 90 GPa. But in all devices the deflection seen at 20 °C and 60 °C was found to be no different (Figure 44).

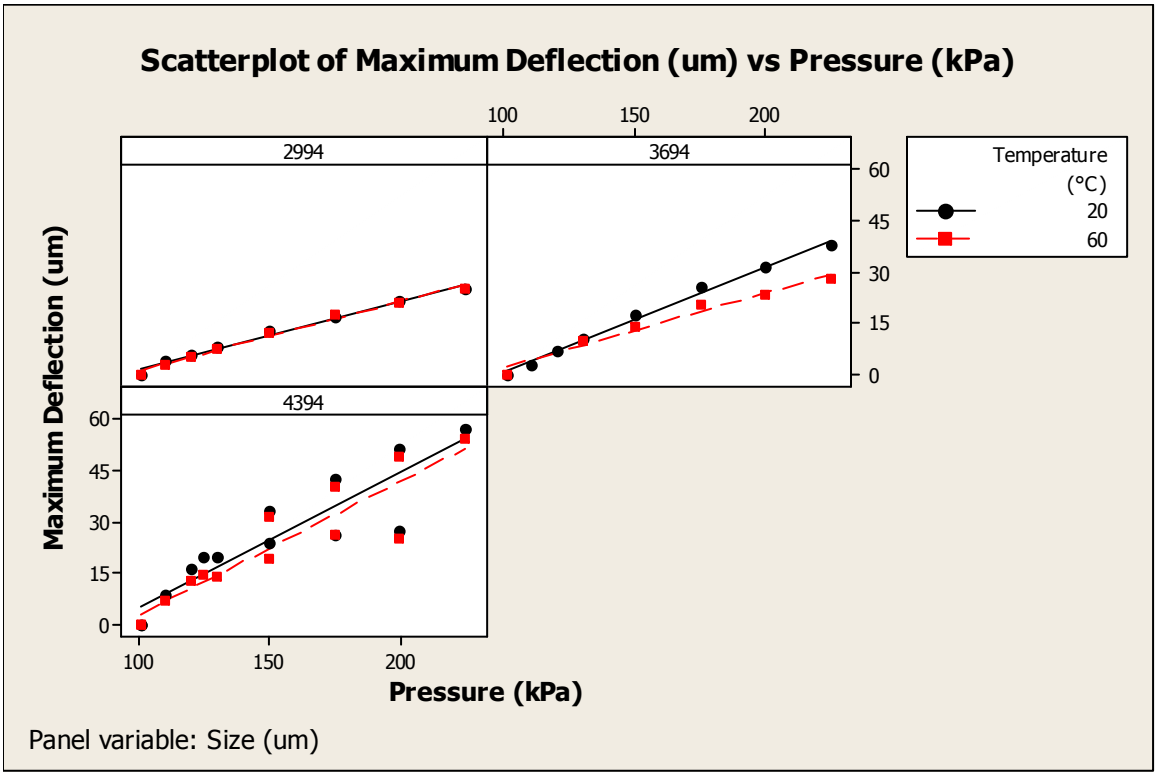

Figure 44: Scatterplot of maximum deflection as a function of pressure showing little to no difference between room temperature and 60 °C.

This could mean the devices were not heat treated properly and were not shape memory or that the austenite finish temperature, and maybe even the austenite start temperature, was above the tested temperature of 60 °C. It should be noted that the thermocouple controlling the heating pad was below the aluminum block. The temperature controller was then attempting to keep the aluminum block at 60 °C and not the device package. It was believed that due to the high thermal conductivity of the aluminum, silicon and NiTi that the majority of the heat was successfully pass to the device. This appeared to not be the case as the device did not act any different between 20 °C and 60 °C. The heating pad was also unable to go above 60 °C without giving off gaseous fumes which would lead to a damaged heating pad. If the heat could even travel

through all the metallic layers, there was also a insulating PDMS layer to pass through. PDMS has a much higher thermal conductivity of 0.15 W/mK. versus the thermal conductivity of aluminum of 237 W/mK.[27] Since the heat treatment was moved from the Rohwedder sputtering system to a new vacuum annealing chamber, a difference in heating and cooling rates could lead a change in shape memory properties. The chamber was much smaller and gave a much lower vacuum which could lead to a higher cooling rate and a lower heating rate which could easily alter the A_f temperature. Further exploration was desired to find the A_f temperature with the new vacuum annealing chamber as well as maybe finding a superior heat treatment.

4.3 Obtaining Shape Memory

The effect of heat treatments on the austenite finish temperature was explored. This was done with a simple 3^2 full factorial. Due to time constrains, only one replication could be done at each point. It was desirable that the design of experiments be centered around the current heat treatment which is 550 °C for 1 hour. It was also desired to have the design balanced. Research showed that a minimum temperature of 450 °C is needed for amorphous NiTi to recrystallize and anneal.[11] This led to the three temperatures to be tested: 450 °C, 550 °C, and 650 °C. The three times used were 0.5 hours, 1 hour, and 1.5 hours. This was chosen due to simplicity and to minimize annealing time. Annealing times above a few hours would take too long and cause the chamber to become too hot and cause degradation of the chamber and the components. These samples were then analyzed using DSC recording the austenite start, austenite peak, austenite finish, martensite start, martensite peak, and martensite finish temperatures following ASTM standard F2004-06. The samples were ripped off the oxide layer and cut into smaller

pieces and measured to be around 1-5 mg. The DSC was then used with an empty aluminum reference pan and the sample aluminum pan with the NiTi sample inside. The range of the scan was -50 ˚C to 200 ˚C with a heating and cooling rate of 10 ˚C/min. The austenite finish temperature is the most important for shape memory, but the same trends were found for all six temperatures recorded. It was found that all samples annealed at 450 °C did not yield shape memory as well as 650 °C for 1.5 hours. The other five samples all had austenite finish temperatures above room temperature (as well as an austenite start temperature above room temperature). There was no significant difference between the various heat treatments and the austenite finish temperature (Figure 45). This agrees with the literature; the austenite finish temperature is influenced more by composition rather than the heat treatment.[18] The heat treatment can change the temperature by a few degrees, but not drastically.[18]

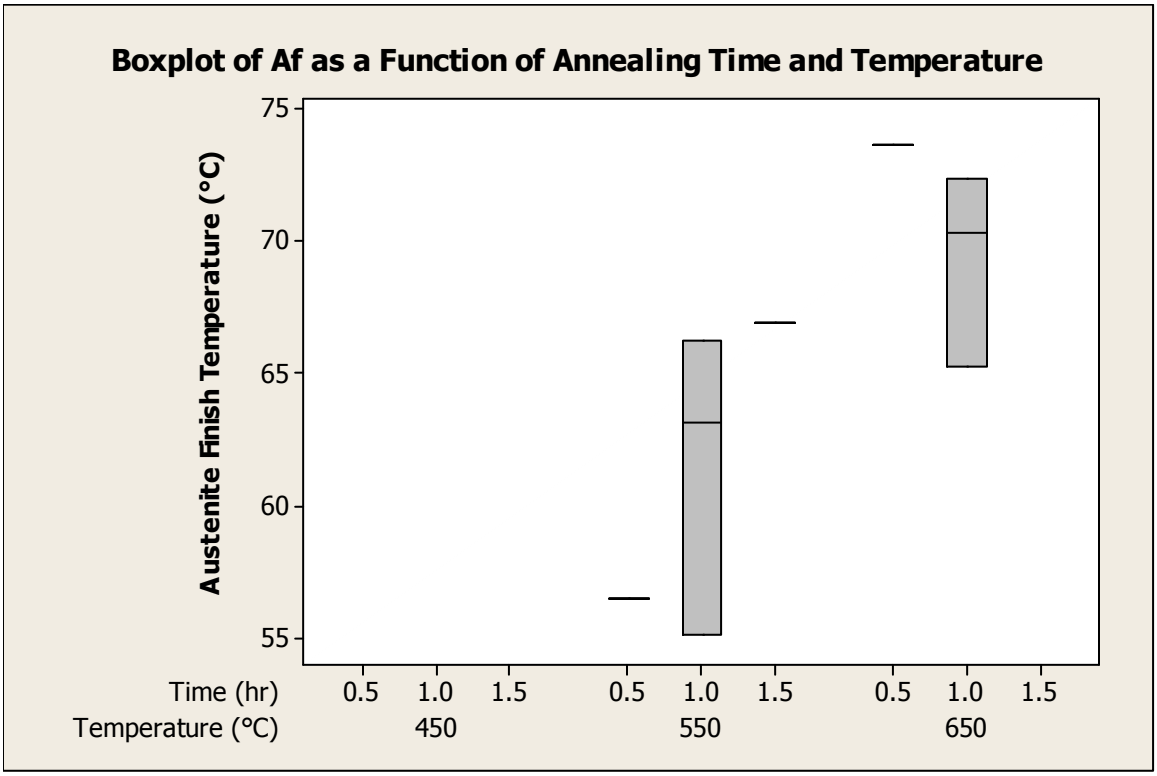

Figure 45: Bar graph showing the austenite finish temperatures for the various heat treatments. All samples at 450 ˚C and the sample at 650 ˚C for 1.5 hours did not show any A_f temperature in the range scanned.

It should be noted that the 550 °C for 1 hour yielded shape memory with an austenite start of 41.58 °C, austenite peak of 45.63 °C, and an austenite finish of 55.09 °C. An additional sample was run in addition to the design of experiments; this sample was heat treated for 550 °C for 1 hour but was pulled out when the sample was cooled to 300 °C and placed on a chill plate. This was done to essentially quench the reaction and stop the precipitation and crystallization process. Previous work found this to yield better results, but ended up resulting in much thicker chromium oxide films. The oxide was desired to be minimized to reduce chromium oxide etching time so all the other samples remained in the heating chamber with the vacuum pump engaged in order to reduce the

amount of oxide grown. No difference was found in any of the phase change temperatures; the difference in A_f was only about 5 °C with an average of 59.11 °C. This was not observed in the devices tested which were heated to 60 °C for 10 minutes prior to testing. Running an analysis on the available data, it was found that each temperature and time as independent variables did not affect the phase change temperatures, but only when combined was there a significant effect. This makes sense as both time and temperature are needed for crystallization and precipitation.

It was found that 650 °C yielded not only shape memory with an austenite finish of 65.25 °C; it had the largest peak and the most defined phase changes detected by the DSC (Figure 46). Though the area below the curve were similar to all the other samples, this more prominent peak means a rapid phase change rather than a prolonged phase change like that observed in other samples (Figure 47). This heat treatment should be more closely examined as a superior heat treatment to the 550 °C for 1 hour.

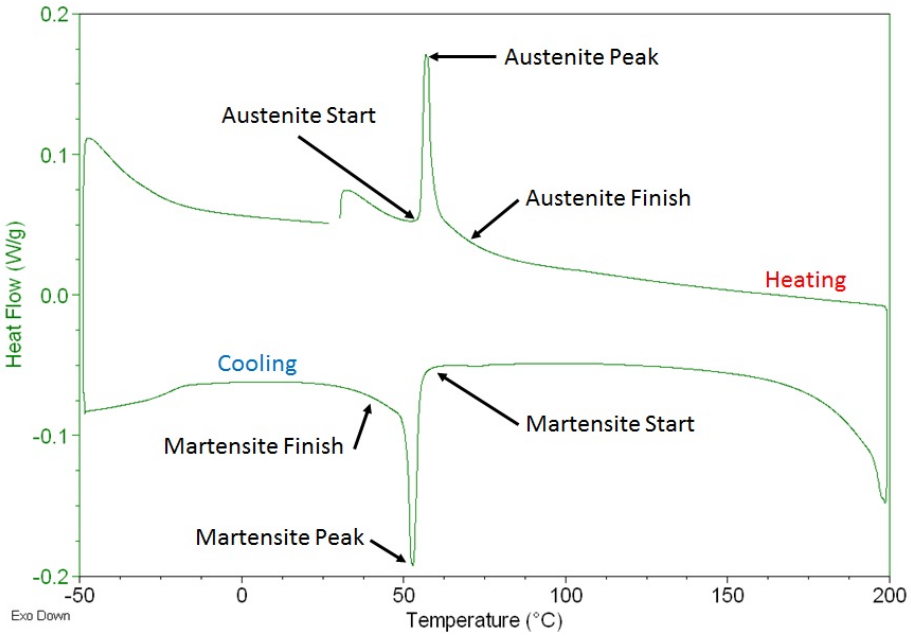

Figure 46: Diagram of the DSC scan on the 650 °C for 1 hour heat treatment. The peaks observed were the most prominent than in any other sample tested.

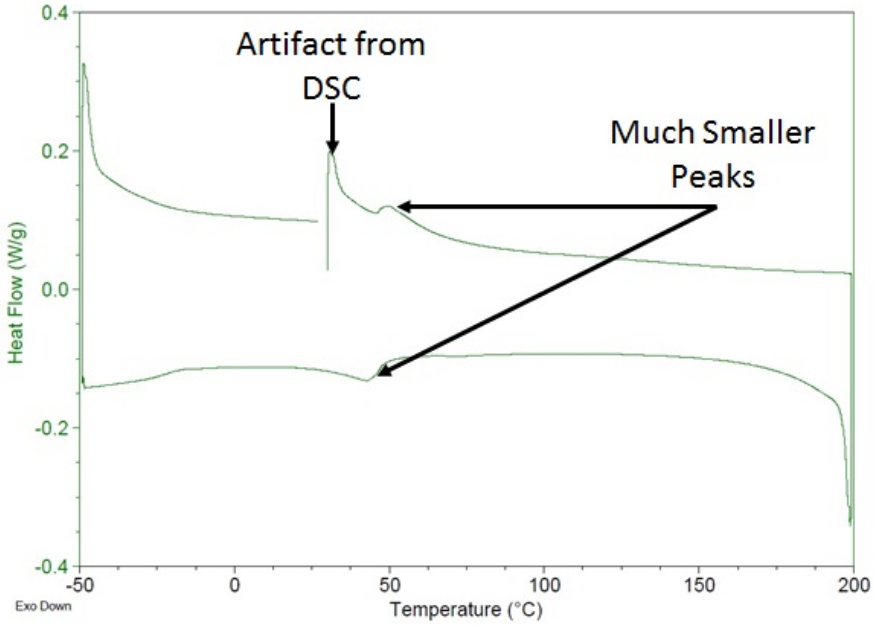

Figure 47: Diagram of the DSC scan on the 550 °C for 1.5 hours heat treatment. The peaks observed are less prominent and broader than the peaks found in the 650 °C for 1 hour heat treatment.

The 650 °C heat treatment yields a stronger peak in the DSC since NiTi is only stable above 630 °C.[36] Since below this temperature NiTi is only metastable below this temperature, crystallizing and precipitation is much more difficult. But above this temperature, NiTi will be more stable which would make crystallization and precipitation process simpler.

Chapter 5 - Conclusions

A thin-film NiTi membrane was able to be fabricated and tested with varying membrane size, pressure, and temperature. This membrane acted similar to theoretical models with some deflecting less and others deflecting more. Shape memory NiTi was not obtained in the devices most likely due to the high stresses of both the sputtering process as well as testing the devices themselves. A design of experiments was conducted in order to find a new and superior heat treatment which was found to be 650 °C for 1 hour. This heat treatment was found to give sharp peaks when looking at the thermal profile using DSC.

Two additional replications of the 650 °C for 1 hour were conducted in order to verify the phase change temperatures as well as better quantify the variability in the processing. The average austenite finish temperature was 69 ± 3.65 °C. A full silicon wafer was cleaned and sputtered with NiTi then chromium following the processes in chapter 3. This wafer was then annealed at 650 °C for 1 hour to verify that no delamination would occur. Previous work by David Getchel indicated that delamination could occur at this temperature, but no indication of delamination was found on the wafer.

Chapter 6 - Future Work

There is much work that could build off the work presented in this paper. More characterization is needed, especially with many more replications. Since this work focused on characterizing the process in which to create a testable device and showed that the device is not only testable, but yields results similar to theoretical models, more replications are easily feasible with more time. More variables should be explored with thickness being the first that comes to mind. Thickness would be simple to change, but would require multiple wafers since a different sputtering time would be needed. Thinner films would lead to less processing time, but would be more fragile. Thicker films would be more structurally sound, but would require much longer sputtering times and characterization of thicker films sputtered on the Rohwedder PVD system have not been done past 5 μm.

As only one replication was done to verify the shape memory heat treatment, more analysis on the influence of the new annealing chamber and how time and temperature affect the A_f temperature are needed. It seems that 650 °C for 1 hour led to the best heat treatment, so more analysis needs to be done on this point as well as around this point to better understand the process. Also, since all the samples tested were cut pieces of silicon, the film delaminated and the influence of the heat treatment on the delamination process needs to be investigated. The film should not delaminate if sputtered onto silicon or chromium due to the much higher adhesion strength; again, this should be investigated.

Processing on p-type wafers should also be investigated in order to be able to bond the wafer to a glass substrate using anodic bonding as described before. Anodic bonding would yield a strong bond with no extra material needed, such as glue. This would lead to a much higher device yield since few devices would be lost during the bonding process due to glue or PDMS leaking into the sealed chamber and preventing deflection of the membrane.

Cyclic testing of the device with an AC current should also be investigated since this is how most micropumps of shape memory NiTi are actuated. Due to the medium resistivity of the NiTi, ohmic heating can easily heat the material past the A_f temperature and with some simple circuitry, the temperature can be well controlled for maximum efficiency.

Making devices like a micropump should also be investigated. The device has been shown to deflect, so if the heat treatment can be properly done and a shape memory device can be fabricated, creation of a micropump is feasable.

The fabrication of a micropump is feasible with the equipment and techniques already examined in this work. The same processes could be used to create the membrane and package the device, with the only difference coming in the need to drill two holes as opposed to one. With the use of two one-way valves liquid would flow into the chamber and deflect the NiTi membrane. This membrane could then be heated with a variety of techniques like ohmic heating, and when heated the membrane would push the liquid out the other one-way valve. New liquid would then flow into the chamber and cool the NiTi as well as deflect the membrane. Another heating cycle would push the new liquid out and this process could be repeated to create a micropump.

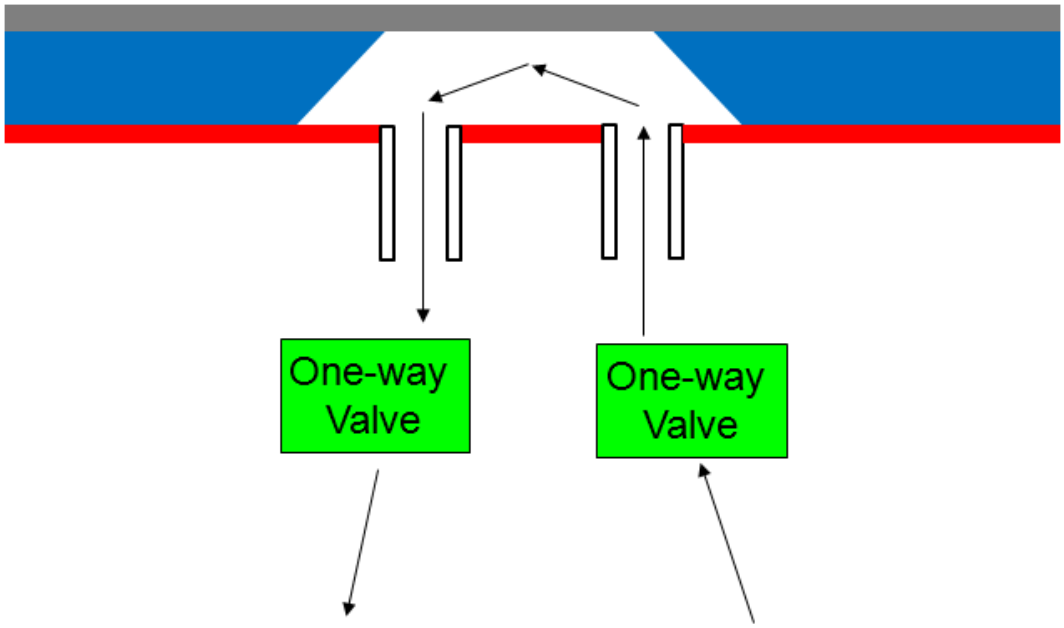

Figure 48: Diagram of a potential NiTi SMA micropump showing the flow of liquid through the device.

References

[1] Shawgo, Rebecca S., Amy C. Richards Grayson, Yawen Li and Michael J. Cima. "BioMEMS for drug delivery." Current Opinion in Solid State and Materials Science 6 (2002). 329-334.

[2] Nisar, A., Nitin Afzulpurkar, Banchong Mahaisavariya, and Adisorn Tuantranont. "MEMS-based micropumps in drug delivery and biomedical applications." Sensors and Actuators B 130 (2008). 917-942.

[3] Tao, Sarah L. and Tejal A. Desai. "Microfabricated drug delivery systems: from particles to pores." Advanced Drug Delivery Reviews 55 (2003). 315-328.

[4] Santini Jr., John T., Amy C. Richards, Rebecca Scheidt, Michael J. Cima and Robert Langer. "Microchips as controlled drug-delivery devices." Angewandte Chemie 39 (2000). 2396-2407.

[5] Teo, Ai Ling, Christopher Shearwood, Kian Chye Ng, Jia Lu, and Shabbir Moochhala. "Transdermal microneedles for drug delivery applications." Materials Science and Engineering B 132 (2006). 151-154.

[6] Tsai, Nan-Chyuan and Sue. "Review of MEMS-based drug delivery and dosing systems." Sensors and Actuators A 134 (2007). 555-564.

[7] Makino, Eiji, Takashi Mitsuya, and Takayki Shibata. "Micromachining of TiNi shape memory thin film for fabrication of micropump." Sensors and Actuators 17 (2000). 251-259.

[8] Shin, Daniel D., Kotekar P. Mohanchandra, and Gregory P. Carman. "Development of hydraulic linear actuator using thin film SMA." Sensors and Actuators A 119 (2005). 151-156.

[9] Krulevitch, Peter, Abraham P. Lee, Philip B. Ramsey, James C. Trevino, Julie Hamilton, and M. Allen Northrup. "Thin film shape memory alloy microactuators." Journal of Microelectromechanical Systems Vol 5, No 4, (1996). 270-282.

[10] Huang, H. "On the selection of shape memory alloys for actuators." Materials and Design 23 (2002). 11-19.

[11] Lewis, Matthew. "Mechanical Properties of Annealed and As-Sputterd Thin Film Nickel Titanium by Nanoindentation." Thesis 2010. California Polytechnic State University, San Luis Obispo.

[12] Getchel, David. “Processing of Freestanding NiTi Shape Memory Thin Film Cantilevers.” Thesis 2007. California Polytechnic State University, San Luis Obispo.

[13] Fu, Yongqing, Hejun Du, Weimin Huang, Sam Zhang, and Min Hu. “TiNi-based thin films in MEMS applications: a review.” Sensors and Actuators A 112 (2004). 395-408.

[14] Duerig, T., A. Pelton, and D. Stöckel. “An averview of nitinol medical applications.” Materials Science and Engineering A 273-275 (1999). 149-160.

[15] Shin, Daniel D., Kotekar P. Mohanchandra, and Gregory P. Carman. “High frequency actuation of thin film NiTi.” Sensors and Actuators A 111 (2004). 166-171.

[16] Buehler W.J., J.W. Gilfrich, and R.C. Wiley. “Effect of low-temperature phase changes on the mechanical proerpties of alloys near composition TiNi.” Journal of Applied Physics 34 (1963). 1475-1477.

[17] Otsuka, K., and X. metallurgy of Ti-Ni-based shape memory alloys.” Progress in Materials Science 50 (2005). 511-678.

[18] Pelton, Alan R., Scott M. Russell, and John DiCello. “The Physical Metallurgy of Nitinol for Medical Applications.” Journal of Materials 2003. 33-37.

[19] Wolf, Richard H. and Arthur H. Heuer. “TiNi (Shape Memory) Films on Silicon for MEMS Applications.” Journal of Microelectromechanical Systems Vol. 4, No. 5, (1995). 206-212.

[20] Dequine, Dustin. “Process Development and Characterization to Manufacture Nickel Titanium Shape Memory Cantilever Micro-Electro-Mechanical Systems.” Thesis 2007. California Polytechnic State University, San Luis Obispo.

[21] Shih, Chen-Luen, Bo-Kuai Lai, Harold Kahn, and Stephen M. Phillips. “A robust co-sputtering fabrication procedure for TiNi shape memory alloys for MEMS.” Journal of Microelectromechanical Systems Vol. 10, No. 1 (2001). 69-79.

[22] Sanjabi, S. and Z.H. Barber. “The effect of film composition on the structure and mechanical proeprties of NiTi shape memory thin films.” Surface and Coatings Technology 204 (2010). 1299-1304.

[23] Ramirez, Ainissa G., Hai Ni and Hoo-Jeong Lee. “Crystallization of amorphous sputtered NiTi thin films.” Materials Science and Engineering A 438-440 (2006). 703-709.

[24] Fu, Yongqing, Hejun Du, and Sam Zhang. “Adhesion and interfacial strcture of magnetron sputtered TiNi films on Si/SiO2 substrate.” Thin Solid Films 444 (2003). 85-90.

[25] Huang, X., Y. Liu, S.F. Ling, H.H. Zhang, and W.M. Huang. “Effect of SiO_2 buffer layer on properties of sputter-deposited NiTi shape memroy alloy thin films.” Surface and Coatings Technology 167 (2003). 148-153.

[26] Stahl, Brian. “Design, Fabrication, Modeling and Characterization of Electrostatically-Actuated Silicon Membranes.” Thesis 2009. California Polytechnic State University, San Luis Obispo.

[27] Campbell, Stephen A. “Fabrication Engieering at the Micro- and Nanoscale.” Third edition. Oxford University Press, Oxford, New York. 2008.

[28] Tabata, Osamu, Ryouji Asahi, Hirofumi Funabashi, Keiichi Shimaoka, and Susumu Sugiyama. “Anisotropic etching of silicon in TMAH solutions.” Sensors and Actuators A 34 (1992). 51-57.

[29] Xu, Dong, Li Wang, Guifu Ding, Yong Zhou, Aibing Yu and Bingchu Cai. “Characteristics and fabrication of NiTi/Si diaphragm micropump.” Sensors and Actuators A 93 (2001). 87-92.

[30] Franssila, Sami. “Introduction to Micro Fabrication.” John Wiley & Sons Ltd., Chichester, West Suxxex, United Kingdom. (2004).

[31] Madou, Marc J. “Fundamentals of Microfabrication: The Science of Miniaturization.” CRC Press Boca Raton, Florida. (2002).

[32] Hsu, Tia-Ran. “MEMS and Microsystems: Design, Manufacture, and Nanoscale Engineering.” John Wiley & Sons Inc. 2008.

[33] Yu, Hongbin, Guangya Zhou, Fook Siong Chau. “Yield improvement for anodic bonding with suspending structure.” Sensors and Actuators A 143 (2008). 462-468.

[34]Lee, Thomas M.H., Debbie H.Y. Lee, Connie Y.N. Liaw, Alex, I.K. Lao, and I-Ming Hsing. “Detailed characterization of anodic bonding processes between glass and thin-film coated silicon substrates.” Sensors and Actuators 86 (2000). 103-107.

[35] Legtenberg, Rob, Henri Jansen, Meint de Boer, and Miko Elwenspoek. “Anisotrpic Reactive Ion Etching of Silicon Using $SF_6/O_2/CHF_3$ Gas Mixtures.” Journal of The Electrochemical Society 142 (1995). 2020-2028.

[36] Chen, Kathy C. "NiTi – Magic or Phase Transformations?" 33rd Annual Frontiers in Education: Engineering as a Human Endeavor: Partnering Community, Academia, Government, and Industry : Conference Proceedings : November 5-8, 2003 : the Westin Hotel, Westminister, Colorado. Champaign, IL: Stipes L.L.C., 2003. Print.